ChemBioChem

Combining Chemistry and Biology

Chemistry Europe

European Chemical Societies Publishing

Cover Feature:

B. Koksch et al.

The Impact of Halogenated Phenylalanine Derivatives on NFGAIL Amyloid Formation

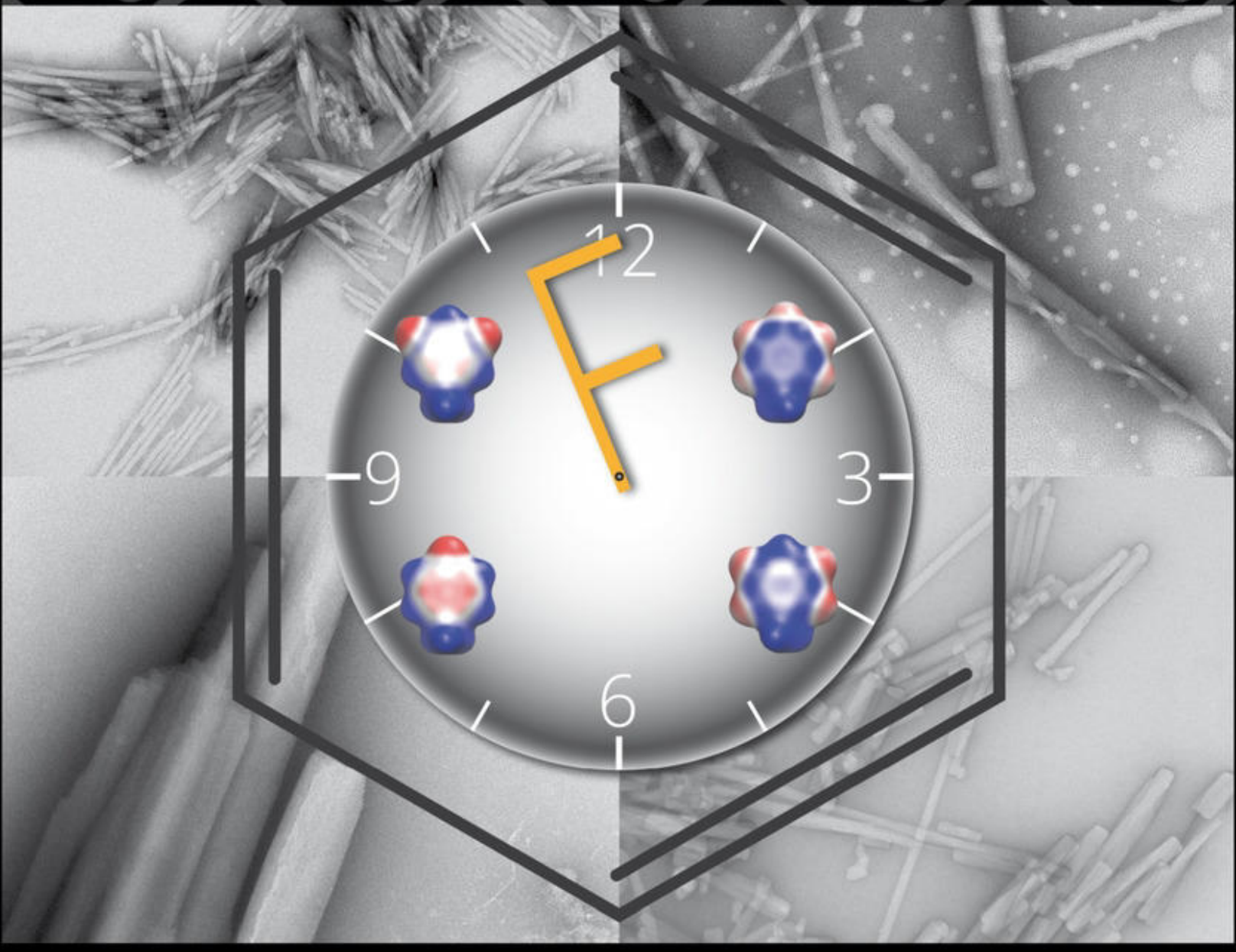

24/2020

WILEY-VCH

Very Important Paper

The Impact of Halogenated Phenylalanine Derivatives on NFGAIL Amyloid Formation

Suvrat Chowdhary,[a] Johann Moschner,[a] Dorian J. Mikolajczak,[a] Maximilian Becker,[b] Andreas F. Thünemann,[c] Claudia Kästner,[c] Damian Klemczak,[d] Anne-Katrin Stegemann,[a] Christoph Böttcher,[e] Pierangelo Metrangolo,[f] Roland R. Netz,[b] and Beate Koksch*[a]

The hexapeptide hIAPP$_{22-27}$ (NFGAIL) is known as a crucial amyloid core sequence of the human islet amyloid polypeptide (hIAPP) whose aggregates can be used to better understand the wild-type hIAPP's toxicity to β-cell death. In amyloid research, the role of hydrophobic and aromatic-aromatic interactions as potential driving forces during the aggregation process is controversially discussed not only in case of NFGAIL, but also for amyloidogenic peptides in general. We have used halogenation of the aromatic residue as a strategy to modulate hydrophobic and aromatic-aromatic interactions and prepared a library of NFGAIL variants containing fluorinated and iodinated phenylalanine analogues. We used thioflavin T staining, transmission electron microscopy (TEM) and small-angle X-ray scattering (SAXS) to study the impact of side-chain halogenation on NFGAIL amyloid formation kinetics. Our data revealed a synergy between aggregation behavior and hydrophobicity of the phenylalanine residue. This study introduces systematic fluorination as a toolbox to further investigate the nature of the amyloid self-assembly process.

Introduction

Native proteins can undergo misfolding and aggregation under conditions of environmental stress.[1] A well-known example are amyloid fibrils, which are pathological signatures of neurodegenerative disorders like Alzheimer's disease (AD), Huntington's disease (HD), Parkinson's disease (PD) and type II diabetes (T2D).[2] In case of T2D, the human islet amyloid polypeptide (hIAPP) aggregates into highly structured amyloid plaques.[3] It is suspected, that hIAPP's toxicity is related to a disruption of the cell membrane of insulin-producing β-cells within the pancreas induced by transient oligomeric aggregates.[4] Several reports studied the complex nature of membrane-associated amyloid formation causing β-cell dysfunction in order to understand the correlation between amyloid growth and cell damage.[5] Thus, an in-depth understanding of the nucleation process of amyloid fibrils is of paramount importance to enable the development of efficient techniques for regulating their kinetics. In 1990, Westermark et al. reported that IAPP-derived amyloids are only formed by humans, cats, and some non-human primates and not observed in case of rodents possessing the rat sequence rIAPP which differs by six amino acids mostly located in the region of residue 20–29.[6] Initial studies revealed hIAPP's amyloidogenicity substantiated in the 20–29 region since the sequence hIAPP$_{20-29}$ (SNNFGAILSS) exposed an amyloidogenic behavior, whereas rIAPP$_{20-29}$ (SNNLGPVLPP) does not form fibrils.[7] Interestingly, Brender et al. studied these sequences in context of membrane disrupting effects and observed membrane fragmentation due to interaction of hIAPP$_{20-29}$ (SNNFGAILSS) with phospholipid bilayers.[5b] Tenidis et al. explored the hexamer hIAPP$_{22-27}$ (NFGAIL) as amyloid core domain, which is assembling into β-sheet-containing amyloid fibrils and possesses a similar cytotoxicity towards the pancreatic cell line RIN5fm as the full-length protein.[8] Among many theoretical[9] and experimental studies[10] about the importance of aromatic residues in amyloid formation, an alanine-scanning mutagenesis experiment[10c] indicated attractive interactions between phenylalanine residues as main driving forces. In addition, previous studies described the onset of early NFGAIL-oligomers by use of ion mobility-mass spectrometry combined with gas-phase IR spectroscopy.[11] Recent articles in amyloid

[a] S. Chowdhary, Dr. J. Moschner, D. J. Mikolajczak, A.-K. Stegemann, Dr. B. Koksch
Institute of Chemistry and Biochemistry
Freie Universität Berlin
Arnimallee 20, 14195 Berlin (Germany)
E-mail: beate.koksch@fu-berlin.de
[b] M. Becker, Dr. R. R. Netz
Department of Physics, Freie Universität Berlin
Arnimallee 14, 14195 Berlin (Germany)
[c] Prof. Dr. A. F. Thünemann, Dr. C. Kästner
Federal Institute for Materials Research and Testing (BAM)
Unter den Eichen 87, 12205 Berlin (Germany)
[d] D. Klemczak
Institute of Pharmacy, Freie Universität Berlin
Königin-Luise-Str. 2–4, 14195 Berlin (Germany)
[e] Dr. C. Böttcher
Institute of Chemistry and Biochemistry and Core Facility BioSupraMol
Freie Universität Berlin
Fabeckstraße 36a, 14195 Berlin (Germany)
[f] Prof. Dr. P. Metrangolo
Department of Chemistry, Materials and Chemical Engineering "Giulio Natta"
Politecnico di Milano
Via L. Mancinelli 7, 20131 Milan (Italy)

Supporting information for this article is available on the WWW under https://doi.org/10.1002/cbic.202000373

This article is part of a Special Collection on Xenobiology. To view the complete collection, visit our homepage

research[12] highlighted the utilization of computational methods to explore the nature of amyloidogenic peptides. In particular, conformational and structural changes of $A\beta_{1-42}$ due to its interaction with toxic gas like CO_2 and NO_2[13] were reported, but also the investigation of membrane binding behaviors of $A\beta_{17-42}$ in different oligomeric states using coarse-grained (CG) MD simulations.[14]

Selective incorporation of fluorinated amino acids is known as a powerful tool to fine-tune biophysical and chemical properties of peptides and proteins.[15] This type of protein engineering has been exploited as a tool to study, for instance, amyloid fibrillogenesis in real-time by ^{19}F NMR spectroscopy combined with CD spectroscopy as reported for the peptides $A\beta_{1-40}$[16] and hIAPP.[17] Incorporation of fluorinated amino acids into amyloidogenic peptides enables to define its impact on the overall fibril structure by probing ^{19}F–^{19}F distances by solid-state ^{19}F NMR spectroscopy.[15d] In general, fluorine has shown to alter important features like hydrophobicity, proteolytic stability and secondary structure propensity of respective amino acids, but this alteration is still difficult to predict.[15d,18] On the other hand, H–F substitution of a phenylalanine side chain leads to a rearrangement of the electrostatic potential (ESP) and, in extreme cases, reverses the quadrupole moment of aromatic systems.[19] This strategy can be used to further elucidate the aggregation process, yet reports of its impact are scarce. The impact of aromatic fluorinated amino acids in amyloid formation was studied by substitution of Phe in $hIAPP_{20-29}$ (SNNFGAILSS) and $hIAPP_{22-29}$ (NFGAILSS).[20] Monofluorination at *para*-position[20b] and, ultimately, perfluorination of the aromatic side chain[20] in these model peptides led to faster aggregation kinetics. However, whether the amyloidogenicity of aromatic residues is due to high hydrophobicity or formation of stabilizing π–π interactions is controversially discussed.[20b,21]

Thus, the state of the art in this field of research called for a systematic study regarding the impact of the aromatic residue on the kinetics of NFGAIL amyloid formation. Our approach was to introduce fluorine and iodine substituents in different numbers and positions into the Phe residue of NFGAIL. A library of NFGAIL variants was prepared, in which Phe is systematically substituted with the selected symmetrical halogenated building blocks [4F]Phe, [3.5F]Phe, [2.3.5.6F]Phe, [2.3.4.5.6F]Phe and [2.3.5.6F][4I]Phe. These sequences were studied by employing thioflavin T fluorescence assays, transmission electron microscopy (TEM) and small-angle X-ray scattering (SAXS).

Results and Discussion

Design of halogenated NFGAIL variants

Although the replacement of carbon-bonded hydrogen with fluorine is generally considered to be isosteric,[22] incorporation of fluorinated amino acids has shown to drastically change the chemical properties of peptides and proteins.[15c,18a] To the best of our knowledge, a hydrophobicity scale for fluorinated analogues of aromatic amino acids a has not been reported yet. In order to establish a suitable indicator of hydrophobicity for the here studied phenylalanine derivatives (Figure 1a), we introduced a condensed-phased plot (Figure 1b) generated by comparison of the retention time of both Fmoc-protected natural and fluorinated amino acids as part of a standardized HPLC assay correlated to computed vdW volumes of their side chains.[23] Also, we calculated corresponding M log *P* values for Phe, [4F]Phe, [2.3.5.6F]Phe, [2.3.4.5.6F]Phe and [2.3.5.6F][4I]Phe as published by Moriguchi et al. (Figure 1c).[24] Both the experimentally determined hydrophobicity scale (Figure 1b) and the calculated M log *P* plot (Figure 1c) confirm an outstanding shift in hydrophobicity and size of the side chain of Phe due to fluorination as shown in Figure 1b, while the extent of fluorination determines the dimension of the change. The presented fluorinated Phe variants can be classified as "*partially fluorinated*" and "*perfluorinated*".

According to the condensed-phased RP-HPLC-assay, partially fluorinated analogues [4F]Phe [t_R (HPLC-assay): 15.44 min], [3.5F]Phe [t_R (HPLC-assay): 16.15 min] and [2.3.5.6F]Phe [t_R (HPLC-assay): 15.81 min] show enhanced hydrophobicity compared to Phe [t_R (HPLC-assay): 14.38 min] but comparatively small differences to themselves, whereas a stronger increase is observed in case of [2.3.5.6F]Phe [t_R (HPLC-assay): 18.57 min] and its iodinated analogue [2.3.5.6F][4I]Phe [t_R (HPLC-assay): 19.99 min]. The latter exhibits the most hydrophobic character combined with the highest vdW volume among all studied Phe variants. Furthermore, recent investigations provided experimental evidence for 4-iodotetrafluorophenylalanine to act as halogen bond-donor, which could also affect amyloid formation.[25] Interestingly, a consistent correlation between a growing degree of side-chain halogenation and increasing hydrophobicity is not fully accounted in case of [2.3.5.6F]Phe. While the HPLC assay depicts slightly weaker hydrophobic properties of the tetrafluorinated Phe variant in contrast to [3.5F]Phe, their M log *P* values appoint an succinctly opposite trend. This is not surprising, since significant differences between both scales exist as they are based on different principles.[26] To overcome this limitation, our group was recently involved in the development of a universal hydrophobicity scale based on clustering of amino acids in the gas phase revealing a unique behavior of fluorinated Phe variants by a decrease in hydrophobicity compared to Phe.[27]

Besides hydrophobicity, π–π interactions have been proposed to play a significant role during amyloid formation in general but several conflicting reports about their importance exist.[21,28] These interactions can be defined as a sum of the interplay between aromatic side chains involving hydrophobic, van der Waals, and also electrostatic forces.[29] They are based on specific types of geometries (*face-face*/*edge-face*) that differ by the angle between two rings and their offset value (Figure 2a).[28b,c] Experimental studies showed a very low amyloidogenic potential in case of the related sequence NYGAILSS and explained this circumstance through a disruption in *face-face*-stacking by the substitution of Phe with Tyr, as molecular dynamics simulations predicted mainly *edge-face* interactions for Tyr-Tyr pairs.[30] In contrast, substitution of Phe with Leu in NFGAIL was reported to retain its amyloidogenic

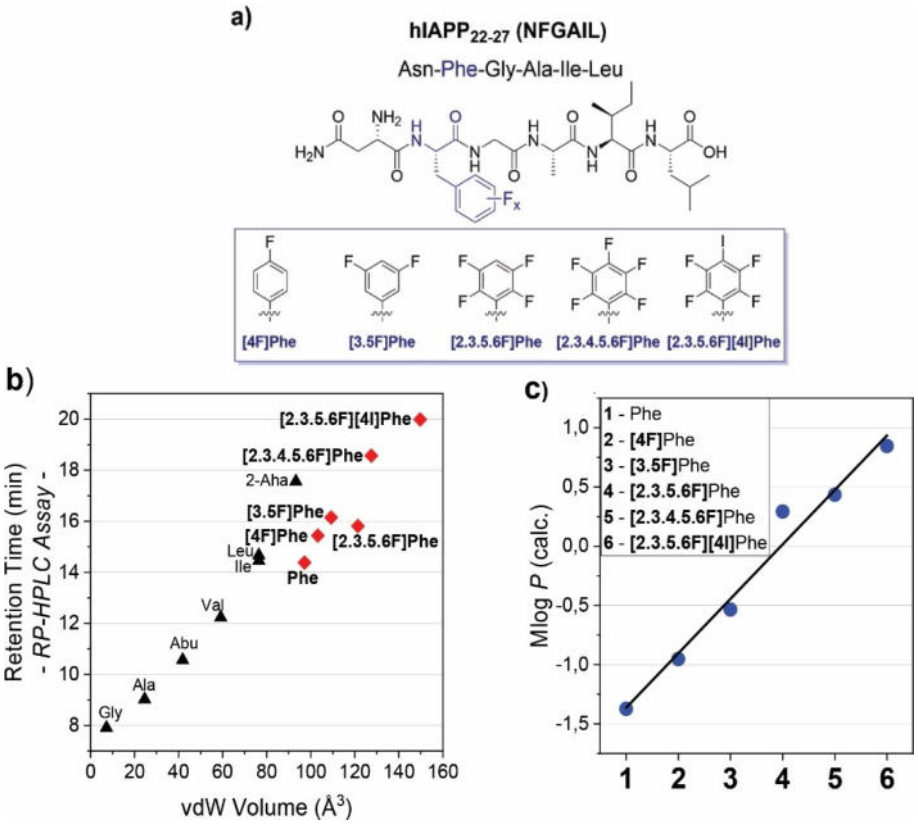

Figure 1. a) Peptide library of halogenated NFGAIL variants. The Phe residue is substituted with the given fluorinated/iodinated analogues. b) Retention times (RP-HPLC assay) of Fmoc-protected amino acids plotted against the vdW volume of their side chains. Phe and its halogenated analogues are represented in red, whereas further native Fmoc-protected amino acids are appearing as black triangles for comparison. The retention time (t_R) of amino acids acts as an experimentally defined dimension of hydrophobicity. c) Hydrophobicity plot based on M log *P* values of native Phe [M log *P*: −1.374],[4F]Phe [M log *P*: −0.953],[3.5F]Phe [M log *P*: −0.535],[2.3.5.6F]Phe [M log *P*: 0.293],[2.3.4.5.6F]Phe [M log *P*: 0.435] and[2.3.5.6F][4I]Phe [M log *P*: 0.846].

behavior.[28a] Herein, the fine-tuned electron density in selected fluorinated phenylalanine analogues allows to gain a deeper insight into occurrences and geometries of aromatic–aromatic interactions in NFGAIL amyloid formation. Calculated electrostatic potential maps of [2.3.5.6F]Phe (Figure 2b,[4]) and [2.3.4.5.6F]Phe (Figure 2b,[5]) highlight the *edge-face* interaction as favored geometry for the tetrafluorinated variant during amyloid formation, whereas *face-face* stacking is expected for the perfluorinated derivative as previously reported for native phenylalanine.[9a,30b,31] It was concluded that the electrophilic H-atom of [2.3.5.6F]Phe at *para*-position could retard the preorganization of amyloid formation kinetics by occupying an *edge-face* geometry, whereas incorporation of the perfluorinated Phe variant [2.3.5.6F]Phe would result in a *face-face* geometry during NFGAIL nucleation. It must be mentioned that during NFGAIL self-assembly, aromatic–aromatic interactions are proposed to act as a tool for preorganization in molecular recognition processes, particularly the association to oligomeric nuclei. Investigation of this part of the self-assembly process gives important information about amyloid nucleation, while structural characterization can define a possible aryl-aryl geometry in solid fibrils formed during the saturation phase. Based on MD simulations[32] and X-ray crystallography experiments[10a] Guo and co-workers and Eisenberg and co-workers reported for hIAPP$_{22–29}$ (NFGAILSS) an orientation of cross-β pattern in the fibril with interactions between Phe and Ile residues of opposite strands. Furthermore, Nielsen and co-workers used solid-state NMR spectroscopy to determine a supramolecular structure for hIAPP$_{20–29}$ (SNNFGAILSS) based on an antiparallel steric zipper type with interacting Phe and Leu residues between two neighboring β-sheets as well as between Phe and Ile of the opposite β-sheet strands.[33]

Thioflavin T fluorescence assay for the detection of NFGAIL amyloid formation

The hexapeptide NFGAIL is capable to form amyloid fibrils at neutral pH.[8] Kinetics of fibril formation were monitored in real-time using thioflavin T staining. We used this method for defining amyloid formation kinetics of the corresponding NFGAIL variants *N*-[4F]Phe-GAIL (Figure 3a), *N*-[3.5F]Phe-GAIL (Figure 3b), *N*-[2.3.5.6F]Phe-GAIL(Figure 3c), *N*-[2.3.5.6F]Phe-GAIL (Figure 3d) and *N*-[2.3.5.6F][4I]Phe-GAIL (Figure 3e). During the lag time, early nuclei formation takes place. An initial step of nucleation consists in the slow and reversible association of monomers. This thermodynamically unfavorable self-assembly process has a high-energy barrier and is the rate-limiting step

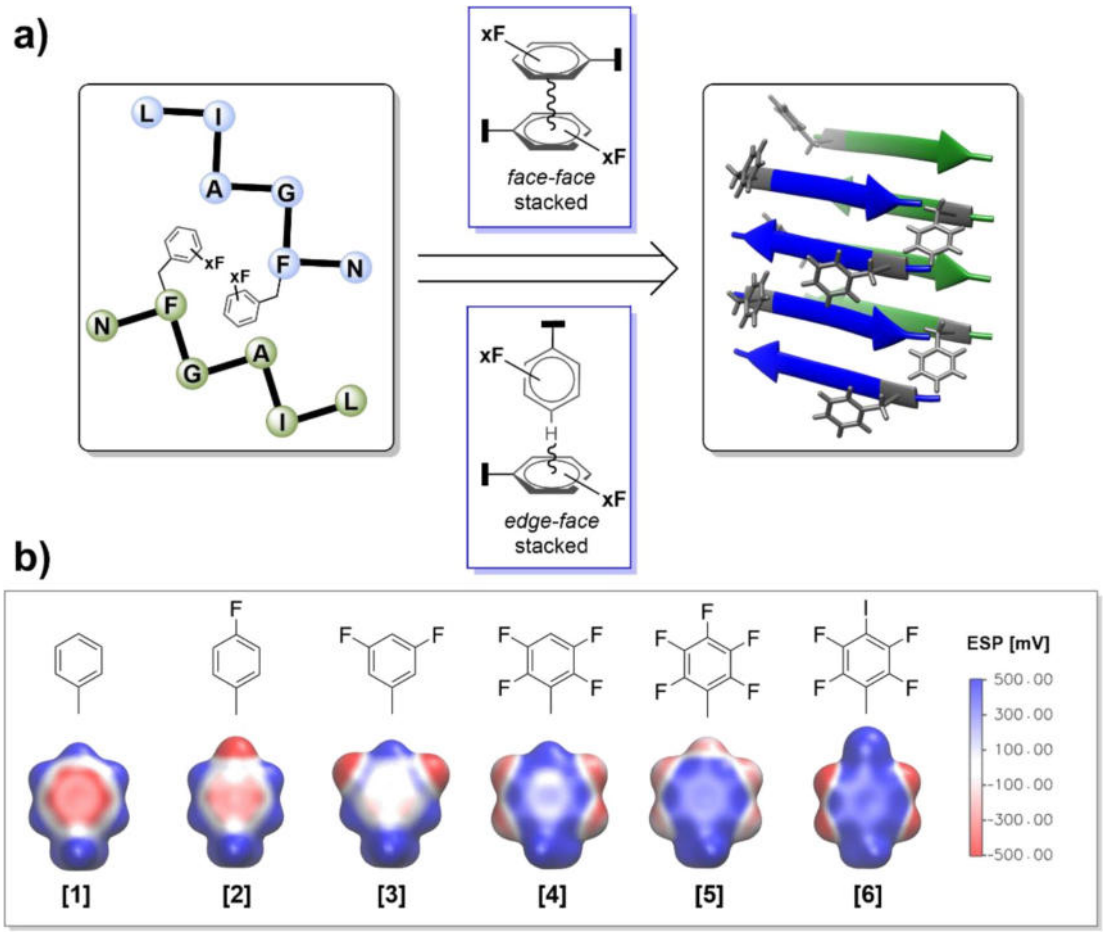

Figure 2. a) Probing the role of π–π interactions as supramolecular driving force in NFGAIL self-assembly with systematic fluorination of aromatic residues. We experimentally studied a possible correlation between the changes in electron density distribution of incorporated phenylalanine derivatives and an alteration of aromatic interactions dring molecular recognition in NFGAIL fibril formation. Aromatic residues predominantly occupy a stacked (*face-face*) or a T-shaped (*edge-face*) geometry. Perturbations in π-stacking geometries were conjectured to provoke interferences in formation of continuous hydrogen-bond-directed β-sheets and therefore affect NFGAIL aggregation kinetics. b) Electrostatic potential (ESP) maps calculated from density-functional theory on interpolated van der Waals radius surfaces (blue means greater or equal the maximum positive potential, red means greater or equal maximum negative potential) of the side-chains of **[1]**phenylalanine and its halogenated derivatives**[2]**[4F]Phe, **[3]**[3.5F]Phe, **[4]**[2.3.5.6F]Phe, **[5]**[2.3.5.6F]Phe and **[6]**[2.3.5.6F][4I]Phe, which were incorporated into NFGAIL.

during the entire aggregation event.[34] All ThT curves show sigmoidal aggregation profiles as a typical feature of nucleation-dependent polymerization mechanism and their lag times are listed in Table 1.[2a,35] Recently, we examined the aggregation kinetics of the native NFGAIL sequence and fibril formation was detected after 20 h at 4 mM and confirmed by visualization of NFGAIL amyloids by transmission electron microscopy.[11]

Table 1. Lag times of halogenated NFGAIL variants determined by ThT fluorescence staining. Errors were obtained as standard deviations of measurements taken from independent experiments. (±SD, $n=3$, further congruent curves can be found in the Supporting Information)

Sequence	Conc. [mM]	Lag time [h]
N-[4F]Phe-GAIL	4	6.00 ± 0.37
N-[3.5F]Phe-GAIL	4	18.16 ± 1.10
N-[2.3.5.6F]Phe-GAIL	4	1.00 ± 0.22
	3	8.33 ± 0.14
N-[2.3.5.6F]Phe-GAIL	3	0.33 ± 0.19
	3	0
N-[2.3.5.6F][4I]Phe-GAIL	1	3.33 ± 0.17

A distinctive critical concentration is an indispensable criterion to initiate fibril formation.[36] Recent studies provided experimental data for a critical-concentration dependency in case of $A\beta_{1-42}$ amyloid aggregation.[37] In contrast, Brender et al. examined the full-length polypeptide hIAPP and determined a lack of concentration-dependency during amyloid aggregation at low initial concentrations, but a significant acceleration in fiber formation near a threshold concentration.[38] Our kinetic data demonstrate a strict concentration-dependency of amyloid formation rates. It can be concluded that the lag time of aggregation significantly decreases with increasing concentration. Thus, a minimal concentration of 4 mM was determined for *N*-[4F]Phe-GAIL and *N*-[3.5F]Phe-GAIL, whereas in analogous experiments at 3 mM concentration formation of aggregates was not detected in time scales of 20–40 h (for all selected concentrations, see Table S1 in the Supporting Information). In

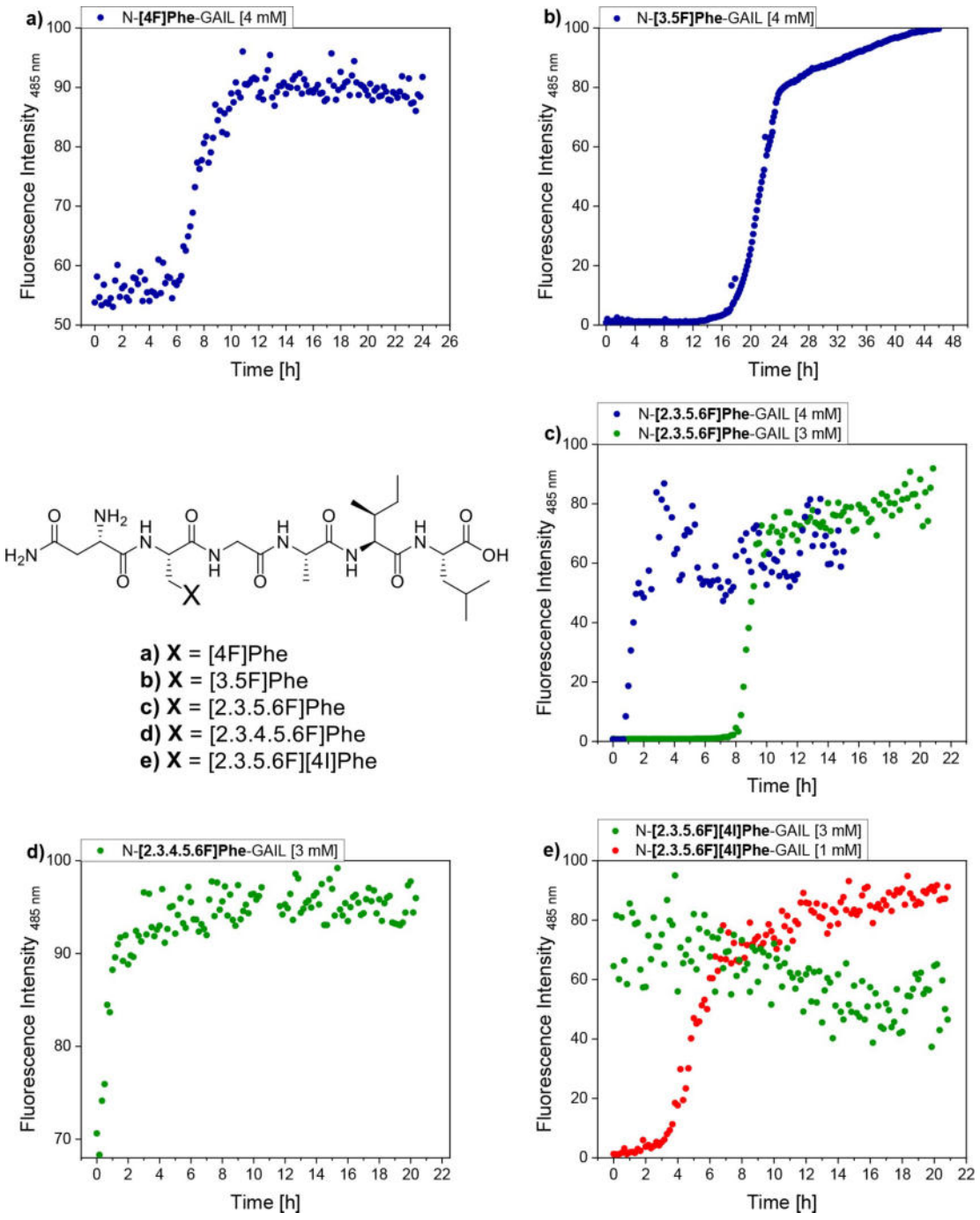

Figure 3. Thioflavin T assays of NFGAIL variants **a)** *N*-[4F]Phe-GAIL,[4 mM] **b)** *N*-[3.5]Phe-GAIL,[4 mM] **c)** *N*-[2.3.5.6F]Phe-GAIL[4 and 3 mM] **d)** *N*-[2.3.5.6F]Phe-GAIL[3 mM] and **e)** *N*-[2.3.5.6F][4I]Phe-GAIL [3 and 1 mM] incubated at 37 °C with orbital shaking for 2 s (amplitude: 2 mm, frequency: 280.8 rpm) before each measurement (10 min intervals) and dissolved in ammonium acetate (10 mM) buffer containing 20 μM thioflavin T, pH 7.0. The fluorescent dye gives a strong fluorescence upon binding to amyloids caused by rotational immobilization. Fluorescence emission was measured at 485 nm and normalized with respect to its maximum value.

comparison, the native sequence NFGAIL follows a nucleation dependent growth mechanism at 4 mM.[11] *N*-[2.3.4.5.6F]Phe-GAIL and *N*-[2.3.5.6F][4I]Phe-GAIL showed lower minimal concentrations (3 mM, 1 mM), whereas higher concentrations led to immediate aggregation. Nevertheless, it must be mentioned that our initial concentrations are very high compared to experimentally defined values for the polypeptide hIAPP (0.5–5 μM)[38] and $hIAPP_{20-29}$ (SNNFGAILSS; 0.25 mM),[33] but in accordance to initial studies of the sequences $hIAPP_{23-27}$ (FGAIL) and $hIAPP_{22-27}$ (NFGAIL; each 5 mM).[8] Also, the nature of the buffer has an impact on the formation of amyloids. For each of the above-mentioned peptides different buffers were used

(hIAPP: 10 mM sodium phosphate buffer, 100 mM NaCl, pH 7.3/ $hIAPP_{20-29}$ (SNNFGAILSS): 50 mM HEPES buffer, pH 7.2/$hIAPP_{23-27}$ (FGAIL) and $hIAPP_{22-27}$ (NFGAIL): 10–20 mM sodium phosphate buffer, pH 7.4/this work [as established by Hoffmann et al.]: 10 mM ammonium acetate, pH 7.0).[8,11,33,38] As recently reported by Brudar et al., buffer specific effects can dramatically affect amyloid self-assembly by stabilizing or disrupting the protein native structure, so that comparison of our results to previously described sequences is difficult.[39]

Our fluorescence data are in accordance to conclusions of theoretical studies and show a correlation between hydrophobicity and amyloid formation rate.[9a,32] *N*-[2.3.5.6F]Phe-GAIL (3 mM; Figure 3d) folds into amyloids much faster than *N*-[4F] Phe-GAIL (4 mM; Figure 3a). These results are consistent to experimental studies reporting an acceleration by incorporation of 2, 3, 4, 5, 6-pentafluorophenylalanine in cognate sequences $hIAPP_{20-29}$ (SNNFGAILSS) and $hIAPP_{22-29}$ (NFGAILSS).[20] At a concentration of 4 mM, the tetrafluorinated variant *N*-[2.3.5.6F] Phe-GAIL (Figure 3c) displayed here faster aggregation kinetics than its monofluorinated and difluorinated derivatives. An immediate aggregation of *N*-[2.3.5.6F][4I]Phe-GAIL (Figure 3e) at a concentration of 3 mM was found, which we explain based on its pronounced hydrophobicity, which is the strongest amount of all here studied phenylalanine derivatives (Figure 4a–b). Therefore, higher values of the "C–I"-bond length and atomic size of iodine compared to fluorine could have led to sterically demanding situations that could have disturbed the aggregation process. Beside hydrophobic interactions also halogen bonding with, for example, the side chain of Asn or the peptide backbone, could affect the preorganization of *N*-[2.3.5.6F][4I] Phe-GAIL in solution and, thus, contribute to NFGAIL fibril formation.

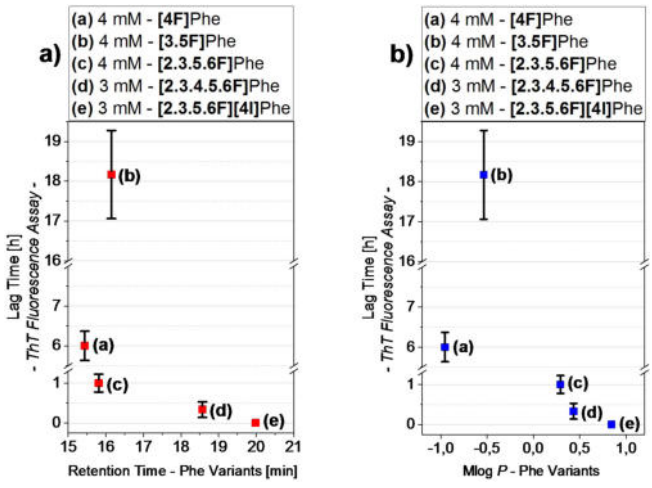

Figure 4. Lag times of halogenated NFGAIL variants were plotted against a) the experimentally determined retention times of incorporated phenylalanine derivatives and b) their calculated M log *P* values. Both plots reveal a correlation between decreased lag times and ehanced hydrophobic properties of the Phe residues due to side-chain halogenation[4F]Phe→[2.3.5.6F] Phe→[2.3.5.6F]Phe→[2.3.5.6F][4I]Phe, which results in accelerated aggregation kinetics.

In terms of aromatic–aromatic interactions, our experimental data do not reveal further information about specific π-stacking geometries. Opposite π-stacking modes (*N*-[2.3.5.6F] Phe-GAIL = *face-face*/*N*-[2.3.5.6F]Phe-GAIL = *edge-face*) were not observed to significantly affect the NFGAIL aggregation process and, therefore, seemed to be less important for fibril formation. It is most noteworthy that in previous studies sterically demanding groups were reported to decelerate aggregation kinetics.[20a] Our results surprisingly reveal an independency of amyloid formation rate to the side chain's size in NFGAIL fibril formation. Moreover, we determined a significant increase in vdW volume by incorporation of fluorine and especially iodine and, at the same time, an acceleration of self-assembly into distinct ordered amyloid fibrils as seen in particular for *N*-[2.3.5.6F][4I]Phe-GAIL and confirmed by transmission electron microscopy.

Modulation of aromatic σ-frameworks: Interaction energies of fluorinated phenylalanine derivatives in water

An interesting exception is constituted by the difluorinated NFGAIL variant *N*-[3,5F]Phe-GAIL (Figure 3b) which showed the longest lag time (18.16 ± 1.10 h) of all here studied NFGAIL analogues. Considering its hydrophobic properties (Figure 4a–b), incorporation of [3,5F]Phe should result in an acceleration of NFGAIL amyloid formation compared to [4F]Phe. We assumed the modulated σ-framework within [3,5F]Phe to possibly serve as a diametrical effect towards the amyloid self-assembly process. Previous computational studies about aromatic carbon-bound fluorine revealed the side chain of [3,5F]Phe as a peculiar pattern by possessing two fluorine atoms able to participate in hydrogen bonding including a very acidic aromatic hydrogen atom at *para*-position.[40] In an aqueous solution, this structure generates adjacent binding sites which could not only facilitate C–H–O interactions known in literature as *non-classical hydrogen bonds (NCHBs)*, but also F–H bridges with water molecules.[40–41] To quantify this argument, we calculated interaction energies of water molecules with the toluene derivatives at zero temperature using density functional theory and post-Hartree-Fock methods. The resulting minimal energy structures and the binding energies are shown in Figure 5 (see computational methods for details). In case of [3,5F]Phe, we find multiple favorable water-binding motifs, stemming from its alternating positively and negatively charged binding sites (Figure 2b). First, we optimized the structure of single water molecules that interact with the fluorinated aromatic systems, the resulting equilibrium geometries are depicted in Figure 5a. It is seen that single water molecule binding to partially fluorinated systems is strongly enhanced by an alternating H–F configuration. There, the water molecule can act as acceptor and donator at the same time (Figure 5a,[2,5]), compared to the water molecule arranging at two fluorine atoms (Figure 5a[6,7]). We see that [3,5F]Phe has a total of four possible strong binding modes of the H–F type (Figure 5a,[3,4] each counted twice with its symmetric counterpart) and thus is suggested to have stronger interactions with water than all the

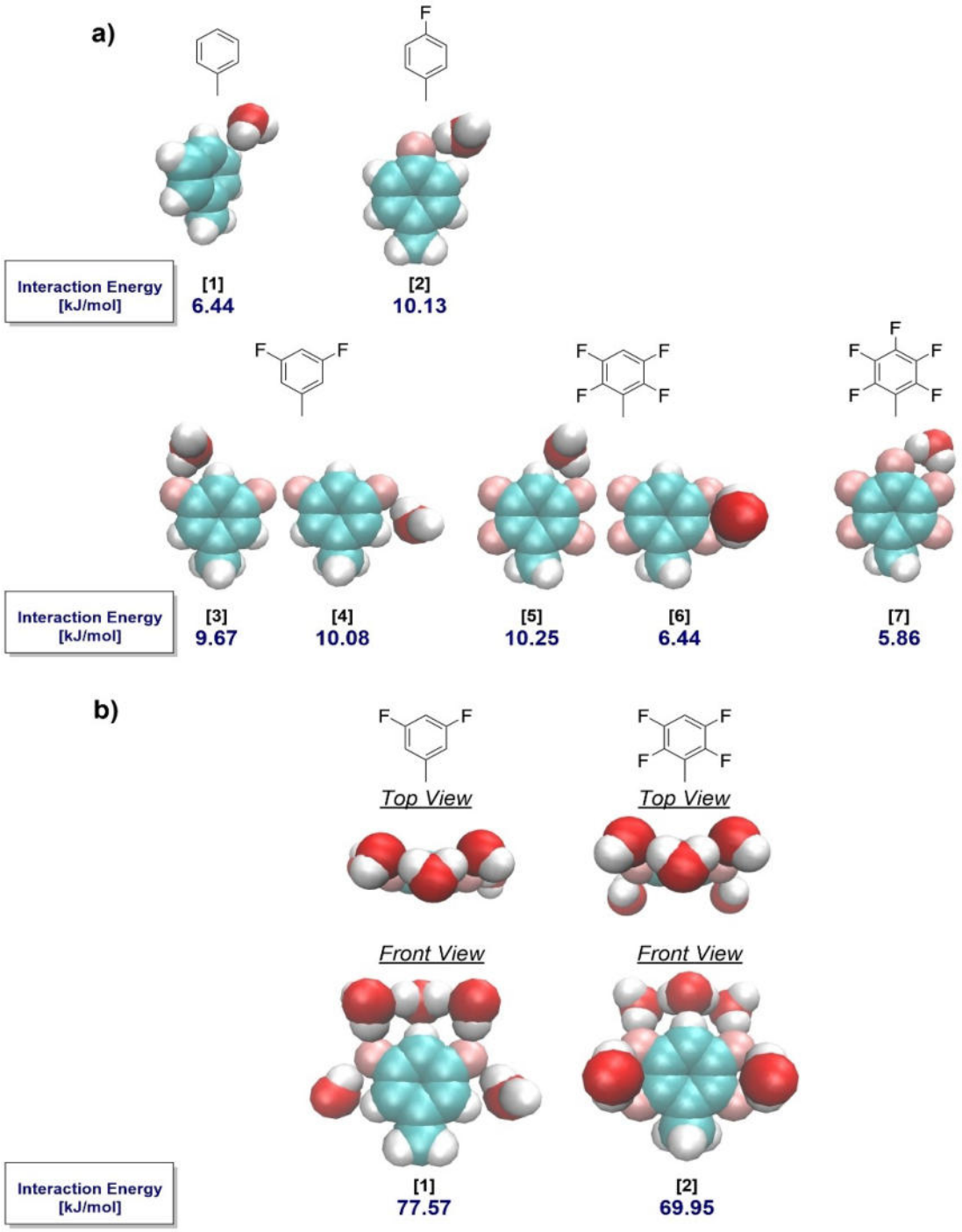

Figure 5. a) Various optimized water-binding geometries of **[1]**phenylalanine and its derivatives**[2]**[4F]Phe, **[3]****[4]**[3.5F]Phe, **[5]****[6]**[2.3.5.6F]Phe and **[7]**[2.3.5.6F] Phe calculated for toluene and its fluorinated derivatives with corresponding complexation energies. b) Calculated *5-water clusters* for **[1]**[3.5F]Phe and **[2]** [2.3.5.6F]Phe.

other compounds. We note that the reported interaction energies are substantially smaller than water-water interaction energies, which we calculated to be 17.15 kJ/mol at the chosen level of theory for two water molecules, indicating that all fluorinated compounds studies here are hydrophobic. The top region of [3,5F]Phe and [2.3.5.6F]Phe with its F–H–F binding motif allows for a specific *3-water cluster* which binds to the aromatic ring while maintaining a hydrogen bond network in between the water molecules (Figure 5b). Therefore, we calculated interaction energies for *5-water cluster* for these two compounds. The complexation energy of the [3.5F]Phe *5-water cluster* (Figure 5b,[1]) is larger by 7.62 kJ/mol then of the corresponding [2.3.5.6F]Phe *5-water cluster* (Figure 5b,[2]), because of the additional two binding sites of H–F type at the

bottom of the structure. Comparably well-structured *5-water clusters* could not be found for the remaining compounds. The outlined energetically favorable hydration patterns of [3.5F]Phe could accommodate for relatively strong interactions with the aqueous buffer, providing an explanation for the retardation of amyloid nucleation.

Determination of the morphology of halogenated NFGAIL fibrils by transmission electron microscopy (TEM)

For structural investigation of resulting fibrils, negative-staining TEM images were recorded for all halogenated NFGAIL-derivatives (Figure 6). Generally, all selected samples show rather linear and tightly packed fibrillary structures, but a unique morphology and diameter due to incorporation of fluorine and iodine. *N*-[3,5F]Phe-GAIL formed filaments that bundle into larger fibrils with a diameter of 168.3 ± 27.5 nm, whereas for *N*-[3,5F]Phe-GAIL (11.5 ± 1.6 nm), *N*-[2.3.5.6F]Phe-GAIL (21.3 ± 6.2 nm), *N*-[2.3.5.6F]Phe-GAIL (27.3 ± 7.7 nm) and *N*-[2.3.5.6F][4I]Phe-GAIL (10.5 ± 1.5 nm) a homogeneous structure was found for a single unit of resulting fibrils, possessing a largely unbranched structure. Obviously, halogenation of the phenylalanine residue changes not only the kinetics of fibril formation but does also affect the aggregate's morphology. Large fibril filaments were detected for *N*-[4F]Phe-GAIL, whereas amyloids composed of *N*-[3,5F]Phe-GAIL with analogue concentrations revealed comparatively thinner fibrils, although an opposite finding could have been expected with regards to the higher vdW volume of [3,5F]Phe compared to [4F]Phe. As the mechanisms of amyloid formation in general are still not fully understood due to the complexity of occurring processes within amyloid fibril formation,[3d,42] detailed interpretations of the structure of amyloids based on TEM images are not possible. Therefore, high-resolution structural studies could provide further fundamental information about the role of aromatic interactions in amyloid fibril formation of these NFGAIL variants.

Small-angle X-ray scattering experiments were proceeded for the native NFGAIL sequence and its fluorinated variants *N*-[2.3.5.6F]Phe-GAIL and *N*-[2.3.5.6F]Phe-GAIL (for full SAXS analysis; Figures S37 and S38). As a result, the amyloid fibrils obtained from both native and fluorinated sequences seem to possess a ribbon-like appearance and are comparable to the values as published for a parallelepiped by Langkilde et al.[43]

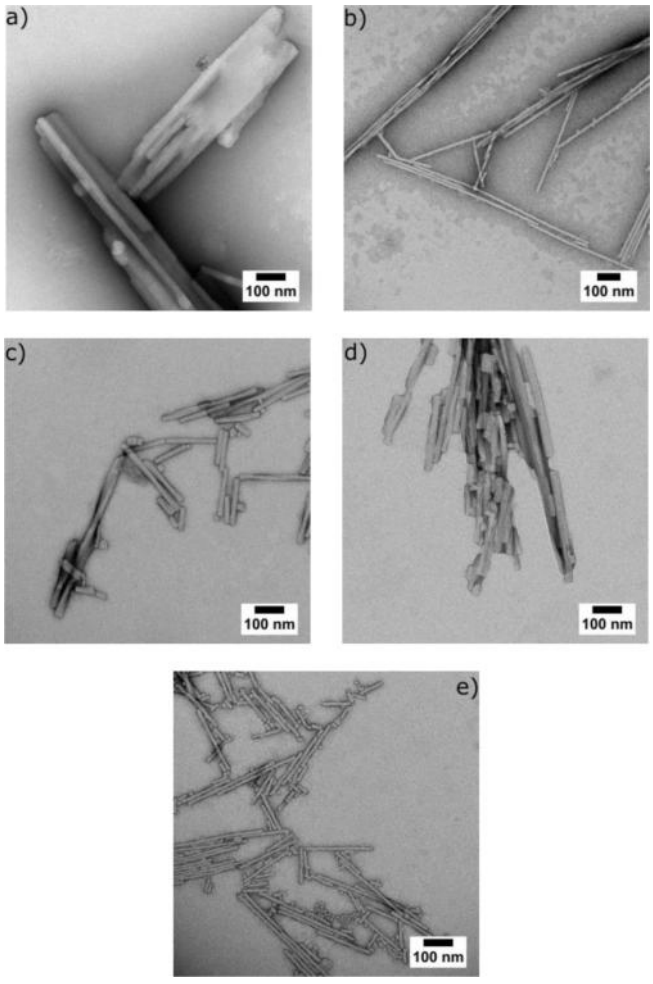

Figure 6. Negative-staining transmission electron microscopy (TEM) images of selected NFGAIL solutions in ammonium acetate buffer (10 mM, pH ~ 7) show the formation of amyloid fibrils. Samples: a) *N*-[4F]Phe-GAIL; [4 mM] b) *N*-[3.5F]Phe-GAIL; [4 mM] c) *N*-[2.3.5.6F]Phe-GAIL; [3 mM] d) *N*-[2.3.5.6F]Phe-GAIL; [3 mM] e) *N*-[2.3.5.6F]Phe-GAIL; [1 mM].

Conclusion

In this study, we presented a series of fluorinated and iodinated analogues of the amyloidogenic model peptide NFGAIL derived from the human islet amyloid polypeptide (hIAPP). We used selective halogenation as a tool to fine-tune the biophysical properties and size of the aromatic residue. As shown through a HPLC-based assay (Figure 1a), calculated M log *P* values (Figure 1b) and ESP maps (Figure 2b), fluorination of the aromatic side- chain leads to an alteration in hydrophobicity and electronic changes in their σ-frameworks. To study the amyloidogenic behavior of halogenated NFGAIL variants, we used ThT fluorescence assay to study amyloid nucleation and propagation, molecular modeling of the fluorinated side chains, but also TEM and SAXS measurements to study the morphology of resulting fibrils. Our kinetic data revealed a synergy between the hydrophobic nature of incorporated Phe analogues and respective aggregation kinetics in NFGAIL amyloid formation. Also, we probed the role of aromatic-aromatic interactions in NFGAIL self-assembly by a possible perturbation of π-stacking geometries and, thus, in molecular self-recognition. Based on our experimental data we suggest an amyloidogenic behavior of these peptides independent from π-stacking geometries. Furthermore, we found a remarkable experimental result given by the elongated lag time of the difluorinated variant *N*-[3.5F] Phe-GAIL, for which, as shown by molecular modeling, we assume its enhanced polarity to act as a diametrical effect towards the amyloid self-assembly process. TEM micrographs revealed specific morphologies and diameters caused by incorporation of fluorine and iodine but confirmed amyloid

formation for all sequences. In addition, SAXS data obtained for the native NFGAIL sequence and its fluorinated derivatives *N*-[2.3.5.6F]Phe-GAIL and *N*-[2.3.5.6F]Phe-GAIL indicated the occurrence of ribbon-like structures that typically resemble amyloid fibrils possessing similar dimensions. The aggregation kinetics of NFGAIL reported herein and the underlying design principle may play a crucial role for future design of amyloidogenic biomaterials or for developing strategies for the inhibition of amyloid formation.

Experimental Section

General methods

^{1}H, ^{13}C and ^{19}F NMR spectra (Figures S1–S12) were recorded at room temperature using a JEOL ECX 400, a JEOL ECP 500 (JEOL, Tokyo, Japan) or a Bruker AVANCE III 700 (700 MHz, Bruker). Chemical shifts δ are reported in ppm with the solvent resonance as the internal standard ($CDCl_3$ = 7.26 ppm, CD_3OD = 3.31 ppm). HRMS were determined on an Agilent 6220 ESI-TOF MS instrument (Agilent Technologies). For analysis, the MassHunter Workstation Software VersionB.02.00 (Agilent Technologies) was used. Fmoc-L-amino acids were purchased from ORPEGEN Peptide Chemicals GmbH (Heidelberg, Germany). Fluorinated Fmoc-L-amino acids were purchased from commercial sources as follows:Fmoc-[4F]Phe-OH (VWR, Darmstadt, Germany), Fmoc-[3.5F]Phe-OH (ABCR, Karlsruhe, Germany), Fmoc-[2.3.4.5.6F]Phe-OH (Oxchem, Wood Dale, USA). Fmoc-[2.3.4.5.6F][4I]Phe-OH was kindly provided by Prof. Dr. Pierangelo Metrangolo. Fmoc-[2.3.4.5.6F]Phe-OH was synthesized according to literature.[19c]

Peptide synthesis

All peptides were synthesized according to standard Fmoc-chemistry using preloaded Fmoc-Leu-NovaSyn®TGA[0.2 mmol/g] resins. Standard couplings were performed in DMF with Fmoc-amino acids and HOBt [1-hydroxybenzotriazole]/DIC [*N*,*N*′-diisocarbodiimide] in eight-fold excess with respect to the resin amount and with double couplings of one hour coupling time. For coupling of fluorinated amino acids, a protocol containing Fmoc-amino acid with HOAt/DIC and COMU/DIPEA with double couplings of 1 h was used. For subsequent capping of free amino groups with acetic anhydride, a solution of Ac_2O (10% (*v/v*) and DIPEA (10% (*v/v*) in DMF (6 mL) was added in three batches. The reaction was then shaken for 3*10 min. Afterwards, resins were washed with 6 mL DMF (3*1 min) and 6 mL CH_2Cl_2 (3 x 1 min). In general, a mixture of DBU [1,8-diazabicyclo[5,4,0] undec-7-en] and piperidine (2% each) in DMF was used for Fmoc-deprotection (3*10 min); the resins were washed between each step with DMF and CH_2Cl_2 (3*6 mL each). Peptides were cleaved from the resin by treatment with TFA/TIPS/H_2O (90:5:5) [1 mL cleavage-cocktail per 50 mg resin] for 3 h using sonication at room temperature. Then the resins were washed thrice with 3 mL TFA and CH_2Cl_2, and excess of solvents were removed by evaporation. Peptides were dried by lyophilization before purification with preparative reversed phase HPLC. For semi-preparative HPLC, all NFGAIL variants were dissolved in MeOH. Purification of synthesized peptides was performed on a Knauer low-pressure HPLC system (Knauer GmbH, Berlin, Germany) sold by VWR, comprising a LaPrep Sigma preparative pump (LP1200), a ternary low-pressure gradient, a dynamic mixing chamber, a 6-port, 3-channel injection valve with an automated preperative 10 mL sample loop, a LaPrep Sigma standard 1-channel UV detector (LP3101), a flow cell of 0.5 mm thickness and a 16-port LaPrep Sigma fractionation valve (LP2016). A Kinetex RPC18 endcapped (5 μM, 100 Å, 250*21.2 mm,

Phenomenex®) HPLC-column was used. A Security GuardTM PREP Cartridge Holder Kit (21.20 mm, ID, Phenomenex®, USA) served as pre-column. As eluents water and ACN, both containing 0.1% (*v/v*) TFA were applied. HPLC runs were performed with a flow rate of 15.0 mL/min, UV detection occurred at 220 nm for respective peptides. A linear gradient of 5–70% ACN + 0.1% TFA was applied within 18 min. Data analysis occurred with an EZChrom Elite-Software (Version 3.3.2 SP2, Agilent). After separation, the purity of the collected fractions was determined by analytical HPLC. Fractions with sufficient purity were combined and ACN was removed by rotary evaporation. Lyophilization of the remaining aqueous solution yielded the pure product. Analytical HPLC was carried out on a Chromaster 600 bar DAD-System with CSM software (VWR/Hitachi). The system works with a low-pressure gradient containing a HPLC-pump (5160) with a 6-channel solvent degaser, an organizer, an autosampler (5260) with a 20 μL sample loop, a column oven (5310) and a diode array flow detector (5430) with a high pressure semi-micro flow cell. A Purospher®STAR RP–C18 endcapped (2 μM, 50*2.1 mm, Merk, Deutschland) UHPLC column was used. Water and ACN, both containing 0.1% (*v/v*) TFA were applied as eluents. A flow rate of 0.6 mL/min was used and the column was heated to 24 °C. UV-detection occurred at 220 nm for respective peptides. A linear gradient of 5–70% ACN + 0.1% TFA within 10 min or 5–100% ACN + 0.1% TFA within 18 min was applied for all NFGAIL variants. The data were analyzed with EZ Chrom ELITE software (version 3.3.2, Agilent). All peptides sequences were obtained as white lyophilized powder: HRMS: NFGAIL = HRMS (ESI-TOF) *m/z*: $[M+H]^+$ calcd. for $C_{30}H_{48}N_7O_8$ 634.3564; found 634.3627. *N*-[4F]Phe-GAIL = HRMS (ESI-TOF) *m/z*: $[M+H]^+$ calcd. for $C_{30}H_{47}FN_7O_8$ 652.3470; found: 652.3475. N-[3,5F]Phe-GAIL = HRMS (ESI-TOF) *m/z*: $[M+H]^+$ calcd. for $C_{30}H_{46}F_2N_7O_8$ 670.3375; found: 670.3392. -[2.3.4.5.6F]Phe-GAIL = HRMS (ESI-TOF) *m/z*: $[M+H]^+$ calcd. for $C_{30}H_{44}F_4N_7O_8$ 706.3187; found: 706.3196. *N*-[2.3.4.5.6F]Phe-GAIL = HRMS (ESI-TOF) *m/z*: $[M+H]^+$ calcd. for $C_{30}H_{43}F_5N_7O_8$ 724.3093; found: 724.3100. *N*-[2.3.4.5.6F][4I]Phe-GAIL = HRMS (ESI-TOF) *m/z*: $[M+H]^+$ calcd. for $C_{30}H_{43}F_4IN_7O_8$ 832.2154; found: 832.2205.

HPLC assay for estimation of hydrophobicity

The protocol for the RP-HPLC assay was previously established by our group.[15d] The retention times of Fmoc-[4F]Phe-OH, Fmoc-[3,5F]Phe-OH, Fmoc-[2.3.4.5.6F]Phe-OH, Fmoc-[2.3.4.5.6F]Phe-OH, Fmoc-[2.3.4.5.6F][4I]Phe-OH and Fmoc-protected native amino acids as reference were determined on a C_{18} column (Capcell C18, 5 μm). The samples were dissolved in 1 mL of a mixture of 40% (*v/v*) ACN in 60% (*v/v*) Milli-Q-water containing 0.1% TFA and filtered over a syringe filter with 0.2 μm pore size. A linear gradient from 40 to 70% ACN over 30 min was applied at room temperature and all experiments were performed in triplicates. The vdW volumes of the side chains were calculated according to Zhao et al.[23b]

Thioflavin T fluorescence assay

As a general procedure, stock solutions of NFGAIL variants were prepared by dissolving the purified peptides in 1,1,1,3,3,3-hexafluoro-propan-2-ol [HFIP] (3–4 mL) and further sonication for 15 min to dissolve all preformed aggregates. Aliquots of these stock solutions were dried and then redissolved in ammonium acetate buffer (10 mM, pH ~ 7), containing 20 μM ThT. The buffer containing ThT was previously filtered over a nylon syringe filter with 0.2 μm pore size. After dissolution, the sample was sonicated for 30 s, transferred on a BRAND® microplate (size: 96 wells, color: black;

Sigma-Aldrich), sealed to prevent evaporation and placed in an Infinite M200 plate reader (Tecan Nordic AB, Molndal, Sweden). ThT fluorescence ($\lambda_{ex}=420$ nm, $\lambda_{em}=485$ nm, Z-position: 15173 nm [manual], gain: 80 [manual], lag time: 0 μs, integration time: 20 μs) was measured every 10 min. The plates were shaken for 2 s (amplitude: 2 mm, frequency: 280.8 rpm) before each measurement and incubated at 37 °C during the whole experiment. The fluorescence intensity at 485 nm was normalized with respect to its maximum value.

Transmission electron microscopy

Aliquots (5 μL) of the aqueous amyloid samples were applied to a Formvar/carbon-covered copper grid (400 mesh, PLANO GmbH, Wetzlar) which was hydrophilized by 60 s glow discharging at 8 W in a BALTEC MED 020 device directly before use. After 45 s of sedimentation, excess liquid was removed with blotting paper and the sample was stained for 45 s using a solution of phosphotungstic acid (PTA, 1%). After excess PTA was removed with blotting paper, the grid was allowed to air dry for at least 30 min. The grid was then transferred to a Talos L120 C transmission electron microscope (FEI Company, Oregon) equipped with a LaB6 electrode operating at an acceleration voltage of 120 kV. Image data were recorded using a 4k×4k Ceta CMOS camera.

Computational methods

Calculation of M log *P* values according to Moriguchi et al. were carried out by using MedChem Designer™ (Simulations Plus Inc., Lancaster, USA).[24,44] All QM density-functional calculations were carried out using Gaussian 16. Geometry optimizations were performed on the B3LYP/6-31(d,p) level of theory; interaction energies were computed from MP2/cc-pVTZ single energy calculations of the optimized structures. All MP2 level computations were corrected for the basis set superposition error using the counterpoise method. Electrostatic potential plots were generated from B3LYP/6-31(d,p) geometry optimized structures by mapping the resulting electrostatic potentials on isosurfaces from volumetric Gaussian density maps generated by the QuickSurf algorithm in *VMD*.

Small-angle X-ray scattering

The SAXS of the samples were performed with a SAXSess camera (Anton Paar, Austria). This Kratky type of camera is attached to a laboratory X-ray generator (PW3830, PANalytical), and is operated with a fine focus glass X-ray tube at 40 kV and 40 mA ($Cu_{K\alpha}$, $\lambda=$ 0.1542 nm). A focusing multi-layer optic and a block collimator provide a monochromatic primary beam with low background. Samples were filled in a reusable vacuum tight flow cell sample holder. SAXS data (intensity as a function of the scattering vector) was recorded for 600 s (60*10 s) with a Mythen detection system (Dectris Inc.) in a q-range of 0.1 to 7.0 nm^{-1} (Anton Paar). The scattering vector is defined in terms of the scattering angle, θ and the wavelength, λ of the radiation, thus $q=4/4\lambda \sin(\theta)$. For clarity, the angle between incident and scattered beam is 2θ. The two-dimensional intensity data was converted to one-dimensional data with SAXSQuant software (Anton Paar). The temperature of 21 °C was controlled with a TCS 120 sample holder (Anton Paar) with an accuracy of ±0.2 °C. A reusable capillary was used for all measurements to attain the same scattering volume and background contribution. The resulting scattering curves were corrected for the contribution of the suspension medium (water) and the capillary. Furthermore, the data was deconvoluted (desmeared) using the length profile of the primary beam[45] with SAXSQuant (Anton Paar AG, Graz). Curve fits using the parallelepiped structure model were performed with the open access SAXS data interpretation program *SASfit*.[46]

Author Contributions

B.K. and J.M. conceived the project and provided guidance on data analysis and interpretation. S.C. designed and performed experiments, analyzed, and interpreted data and wrote the manuscript. D.J.M performed TEM measurements. M.B. performed calculations, analyzed, and interpreted data. D.K. and A.-K.S. performed experiments. A.F.T. and C.K. performed SAXS experiments. C.B. and R.R.N. provided expertise and feedback. P.M. provided reagents.

Acknowledgements

S.C., M.B. and R.R.N. gratefully acknowledges financial support by the Deutsche Forschungsgemeinschaft (DFG) through the collaborative research center CRC-1349 "Fluorine-Specific Interactions", project no 387284271. J.M., R.R.N. received funding by the DFG grant CRC 1114 "Scaling Cascades in Complex Systems", project no. 235221301, project (B03) "Multilevel coarse graining of multiscale problems". D.J.M. received funding from the Deutsche Umweltstiftung. We thank Prof. Dr. Christof Schütte and Dr. Vedat Durmaz for providing the β-sheet structure model (Figure 2a). We thank Dr. Kristin Folmert for preliminary work. We would like to acknowledge the assistance of the Core Facility BioSupraMol supported by the DFG. The authors acknowledge the North-German Supercomputing Alliance (HLRN) for providing HPC resources that have contributed to the research results reported in this paper. Open access funding enabled and organized by Projekt DEAL.

Conflict of Interest

The authors declare no conflict of interest.

Keywords: beta-amyloid fibrils · fluorescence · fluorinated phenylalanine · fluorine · NFGAIL

[1] a) N. Berner, K.-R. Reutter, D. H. Wolf, *Annu. Rev. Biochem.* **2018**, *87*, 751–782; b) F. Chiti, C. M. Dobson, *Annu. Rev. Biochem.* **2006**, *75*, 333–366.
[2] a) J. Adamcik, R. Mezzenga, *Angew. Chem. Int. Ed.* **2018**, *57*, 8370–8382; *Angew. Chem.* **2018**, *130*, 8502–8515; b) R. Riek, D. S. Eisenberg, *Nature* **2016**, *539*, 227.
[3] a) A. Kapurniotu, *BIOspektrum* **2012**, *18*, 734–736; b) R. Nelson, M. R. Sawaya, M. Balbirnie, A. Ø. Madsen, C. Riekel, R. Grothe, D. Eisenberg, *Nature* **2005**, *435*, 773–778; c) A. Kapurniotu, *Pept. Sci.* **2001**, *60*, 438–459; d) M. Krampert, J. Bernhagen, J. Schmucker, A. Horn, A. Schmauder, H. Brunner, W. Voelter, A. Kapurniotu, *Chem. Biol.* **2000**, *7*, 855–871.
[4] a) J. R. Brender, D. L. Heyl, S. Samisetti, S. A. Kotler, J. M. Osborne, R. R. Pesaru, A. Ramamoorthy, *Phys. Chem. Chem. Phys.* **2013**, *15*, 8908–8915; b) J. Janson, R. H. Ashley, D. Harrison, S. McIntyre, P. C. Butler, *Diabetes* **1999**, *48*, 491–498.
[5] a) M. F. M. Sciacca, R. Chillemi, S. Sciuto, V. Greco, C. Messineo, S. A. Kotler, D.-K. Lee, J. R. Brender, A. Ramamoorthy, C. La Rosa, D. Milardi, *Biochimie* **2018**, *1860*, 1793–1802; b) J. R. Brender, U. H. N. Dürr, D. Heyl, M. B. Budarapu, A. Ramamoorthy, *Biochim. Biophys. Acta Biomembr.*

2007, *1768*, 2026–2029; c) J. R. Brender, E. L. Lee, M. A. Cavitt, A. Gafni, D. G. Steel, A. Ramamoorthy, *J. Am. Chem. Soc.* **2008**, *130*, 6424–6429; d) R. P. R. Nanga, J. R. Brender, S. Vivekanandan, A. Ramamoorthy, *Biochim. Biophys. Acta* **2011**, *1808*, 2337–2342; e) D. C. Rodriguez Camargo, K. J. Korshavn, A. Jussupow, K. Raltchev, D. Goricanec, M. Fleisch, R. Sarkar, K. Xue, M. Aichler, G. Mettenleiter, A. K. Walch, C. Camilloni, F. Hagn, B. Reif, A. Ramamoorthy, *eLife* **2017**, *6*, e31226.

[6] P. Westermark, U. Engström, K. H. Johnson, G. T. Westermark, C. Betsholtz, *Proc. Natl. Acad. Sci. USA* **1990**, *87*, 5036–5040.

[7] a) G. G. Glenner, E. David Eanes, C. A. Wiley, *Biochem. Biophys. Res. Commun.* **1988**, *155*, 608–614; b) P. T. Lansbury, *Biochemistry* **1992**, *31*, 6865–6870; c) C. Betsholtz, L. Christmansson, U. Engström, F. Rorsman, V. Svensson, K. H. Johnson, P. Westermark, *FEBS Lett.* **1989**, *251*, 261–264.

[8] K. Tenidis, M. Waldner, J. Bernhagen, W. Fischle, M. Bergmann, M. Weber, M.-L. Merkle, W. Voelter, H. Brunner, A. Kapurniotu, *J. Mol. Biol.* **2000**, *295*, 1055–1071.

[9] a) C. Wu, H. Lei, Y. Duan, *Biophys. J.* **2005**, *88*, 2897–2906; b) C. Wu, H. Lei, Y. Duan, *Biophys. J.* **2004**, *87*, 3000–3009; c) C. Wu, H. Lei, Z. Wang, W. Zhang, Y. Duan, *Biophys. J.* **2006**, *91*, 3664–3672; d) Z. Cai, J. Li, C. Yin, Z. Yang, J. Wu, R. Zhou, *J. Phys. Chem. B* **2014**, *118*, 48–57; e) A. Melquiond, J.-C. Gelly, N. Mousseau, P. Derreumaux, *J. Chem. Phys.* **2007**, *126*, 065101; f) D. Zanuy, B. Ma, R. Nussinov, *Biophys. J.* **2003**, *84*, 1884–1894.

[10] a) A. B. Soriaga, S. Sangwan, R. Macdonald, M. R. Sawaya, D. Eisenberg, *THEOCHEM* **2016**, *120*, 5810–5816; b) W. Deng, A. Cao, L. Lai, *Protein Sci.* **2008**, *17*, 1102–1105; c) R. Azriel, E. Gazit, *J. Biol. Chem.* **2001**, *276*, 34156–34161.

[11] W. Hoffmann, K. Folmert, J. Moschner, X. Huang, H. von Berlepsch, B. Koksch, M. T. Bowers, G. von Helden, K. Pagel, *J. Am. Chem. Soc.* **2018**, *140*, 244–249.

[12] P. H. Nguyen, P. Derreumaux, *Biophys. Chem.* **2020**, *264*, 106421.

[13] V. Saranya, P. V. Mary, S. Vijayakumar, R. Shankar, *Biophys. Chem.* **2020**, *263*, 106394.

[14] S. Y. Cheng, Y. Cao, M. Rouzbehani, K. H. Cheng, *Biophys. Chem.* **2020**, *260*, 106355.

[15] a) C. Jäckel, B. Koksch, *Eur. J. Org. Chem.* **2005**, *2005*, 4483–4503; b) C. Jäckel, M. Salwiczek, B. Koksch, *Angew. Chem. Int. Ed.* **2006**, *45*, 4198–4203; *Angew. Chem.* **2006**, *118*, 4305–4309; c) M. Salwiczek, E. K. Nyakatura, U. I. M. Gerling, S. Ye, B. Koksch, *Chem. Soc. Rev.* **2012**, *41*, 2135–2171; d) U. I. M. Gerling, M. Salwiczek, C. D. Cadicamo, H. Erdbrink, C. Czekelius, S. L. Grage, P. Wadhwani, A. S. Ulrich, M. Behrends, G. Haufe, B. Koksch, *Chem. Sci.* **2014**, *5*, 819–830; e) J. Leppkes, T. Hohmann, B. Koksch, *J. Fluorine Chem.* **2020**, *232*, 109453.

[16] Y. Suzuki, J. R. Brender, M. T. Soper, J. Krishnamoorthy, Y. Zhou, B. T. Ruotolo, N. A. Kotov, A. Ramamoorthy, E. N. G. Marsh, *Biochemistry* **2013**, *52*, 1903–1912.

[17] Y. Suzuki, J. R. Brender, K. Hartman, A. Ramamoorthy, E. N. G. Marsh, *Biochemistry* **2012**, *51*, 8154–8162.

[18] a) A. A. Berger, J.-S. Völler, N. Budisa, B. Koksch, *Acc. Chem. Res.* **2017**, *50*, 2093–2103; b) J. Moschner, V. Stulberg, R. Fernandes, S. Huhmann, J. Leppkes, B. Koksch, *Chem. Rev.* **2019**, *119*, 10718–10801; c) R. Smits, B. Koksch, *Curr. Enzyme Inhib.* **2006**, *6*, 1483–1498; d) S. Huhmann, B. Koksch, *Eur. J. Org. Chem.* **2018**, *2018*, 3667–3679.

[19] a) C. J. Pace, J. Gao, *Acc. Chem. Res.* **2013**, *46*, 907–915; b) C. J. Pace, H. Zheng, R. Mylvaganam, D. Kim, J. Gao, *Angew. Chem. Int. Ed.* **2012**, *51*, 103–107; *Angew. Chem.* **2012**, *124*, 107–111; c) H. Zheng, K. Comeforo, J. Gao, *J. Am. Chem. Soc.* **2009**, *131*, 18–19.

[20] a) T. M. Doran, A. J. Kamens, N. K. Byrnes, B. L. Nilsson, *Proteins Struct. Funct. Bioinf.* **2012**, *80*, 1053–1065; b) A. A. Profit, V. Felsen, J. Chinwong, E.-R. E. Mojica, R. Z. B. Desamero, *Protein Sci.* **2013**, *81*, 690–703.

[21] E. Gazit, *The FASEB Journal* **2002**, *16*, 77–83.

[22] G. A. Patani, E. J. LaVoie, *Chem. Rev.* **1996**, *96*, 3147–3176.

[23] a) S. A. Samsonov, M. Salwiczek, G. Anders, B. Koksch, M. T. Pisabarro, *J. Phys. Chem. B* **2009**, *113*, 16400–16408; b) Y. H. Zhao, M. H. Abraham, A. M. Zissimos, *J. Org. Chem.* **2003**, *68*, 7368–7373; c) S. Huhmann, E. K. Nyakatura, H. Erdbrink, U. I. M. Gerling, C. Czekelius, B. Koksch, *J. Fluorine Chem.* **2015**, *175*, 32–35.

[24] I. Moriguchi, S. Hirono, Q. Liu, I. Nakagome, Y. Matsushita, *Chem. Pharm. Bull.* **1992**, *40*, 127–130.

[25] G. Bergamaschi, L. Lascialfari, A. Pizzi, M. I. Martinez Espinoza, N. Demitri, A. Milani, A. Gori, P. Metrangolo, *Chem. Commun.* **2018**, *54*, 10718–10721.

[26] a) G. Rose, A. Geselowitz, G. Lesser, R. Lee, M. Zehfus, *Science* **1985**, *229*, 834–838; b) C. T. Mant, J. M. Kovacs, H.-M. Kim, D. D. Pollock, R. S. Hodges, *Pept. Sci.* **2009**, *92*, 573–595.

[27] W. Hoffmann, J. Langenhan, S. Huhmann, J. Moschner, R. Chang, M. Accorsi, J. Seo, J. Rademann, G. Meijer, B. Koksch, M. T. Bowers, G. von Helden, K. Pagel, *Angew. Chem. Int. Ed.* **2019**, *58*, 8216–8220.

[28] a) S. M. Tracz, A. Abedini, M. Driscoll, D. P. Raleigh, *Biochemistry* **2004**, *43*, 15901–15908; b) I. M. Stanković, D. M. Božinovski, E. N. Brothers, M. R. Belić, M. B. Hall, S. D. Zarić, *Cryst. Growth Des.* **2017**, *17*, 6353–6362; c) P.-N. Cheng, J. D. Pham, J. S. Nowick, *J. Am. Chem. Soc.* **2013**, *135*, 5477–5492; d) M. R. Sawaya, S. Sambashivan, R. Nelson, M. I. Ivanova, S. A. Sievers, M. I. Apostol, M. J. Thompson, M. Balbirnie, J. J. W. Wiltzius, H. T. McFarlane, A. Ø. Madsen, C. Riekel, D. Eisenberg, *Nature* **2007**, *447*, 453.

[29] a) M. L. Waters, *Curr. Opin. Chem. Biol.* **2002**, *6*, 736–741; b) M. L. Waters, *Biopolymers* **2004**, *76*, 435–445.

[30] a) Y. Porat, A. Stepensky, F.-X. Ding, F. Naider, E. Gazit, *Biopolymers* **2003**, *69*, 161–164; b) R. Chelli, F. L. Gervasio, P. Procacci, V. Schettino, *J. Am. Chem. Soc.* **2002**, *124*, 6133–6143.

[31] G. B. McGaughey, M. Gagné, A. K. Rappé, *J. Biol. Chem.* **1998**, *273*, 15458–15463.

[32] J. Guo, Y. Zhang, L. Ning, P. Jiao, H. Liu, X. Yao, *Biochim. Biophys. Acta* **2014**, *1840*, 357–366.

[33] J. T. Nielsen, M. Bjerring, M. D. Jeppesen, R. O. Pedersen, J. M. Pedersen, K. L. Hein, T. Vosegaard, T. Skrydstrup, D. E. Otzen, N. C. Nielsen, *Angew. Chem. Int. Ed.* **2009**, *48*, 2118–2121; *Angew. Chem.* **2009**, *121*, 2152–2155.

[34] P. Arosio, T. P. J. Knowles, S. Linse, *Phys. Chem. Chem. Phys.* **2015**, *17*, 7606–7618.

[35] C. Iannuzzi, G. Irace, I. Sirangelo, *Molecules* **2015**, *20*, 2510.

[36] a) D. Kashchiev, R. Cabriolu, S. Auer, *J. Am. Chem. Soc.* **2013**, *135*, 1531–1539; b) L. M. Blancas-Mejía, P. Misra, M. Ramirez-Alvarado, *Biochemistry* **2017**, *56*, 757–766; c) A. Lomakin, D. B. Teplow, D. A. Kirschner, G. B. Benedek, *Proc. Natl. Acad. Sci. USA* **1997**, *94*, 7942–7947.

[37] M. Novo, S. Freire, W. Al-Soufi, *Sci. Rep.* **2018**, *8*, 1783.

[38] J. R. Brender, J. Krishnamoorthy, M. F. M. Sciacca, S. Vivekanandan, L. D'Urso, J. Chen, C. La Rosa, A. Ramamoorthy, *J. Phys. Chem. B* **2015**, *119*, 2886–2896.

[39] S. Brudar, B. Hribar-Lee, *Biomol. Eng.* **2019**, *9*, 65.

[40] A. V. Razgulin, S. Mecozzi, *J. Med. Chem.* **2006**, *49*, 7902–7906.

[41] R. C. Johnston, P. H.-Y. Cheong, *Org. Biomol. Chem.* **2013**, *11*, 5057–5064.

[42] a) P. Cao, A. Abedini, D. P. Raleigh, *Curr. Opin. Struct. Biol.* **2013**, *23*, 82–89; b) P. Cao, P. Marek, H. Noor, V. Patsalo, L.-H. Tu, H. Wang, A. Abedini, D. P. Raleigh, *FEBS Lett.* **2013**, *587*, 1106–1118; c) R. Aleksis, F. Oleskovs, K. Jaudzems, J. Pahnke, H. Biverstål, *Biochimie* **2017**, *140*, 176–192.

[43] A. E. Langkilde, K. L. Morris, L. C. Serpell, D. I. Svergun, B. Vestergaard, *Acta Crystallogr.* **2015**, *71*, 882–895.

[44] R. Mannhold, G. I. Poda, C. Ostermann, I. V. Tetko, *J. Pharm. Sci.* **2009**, *98*, 861–893.

[45] D. Orthaber, A. Bergmann, O. Glatter, *J. Appl. Crystallogr.* **2000**, *33*, 218–225.

[46] I. Bressler, J. Kohlbrecher, A. F. Thunemann, *J. Appl. Crystallogr.* **2015**, *48*, 1587–1598.

Manuscript received: June 10, 2020
Revised manuscript received: July 31, 2020
Accepted manuscript online: July 31, 2020
Version of record online: September 23, 2020

ChemBioChem

Supporting Information

The Impact of Halogenated Phenylalanine Derivatives on NFGAIL Amyloid Formation

Suvrat Chowdhary, Johann Moschner, Dorian J. Mikolajczak, Maximilian Becker, Andreas F. Thünemann, Claudia Kästner, Damian Klemczak, Anne-Katrin Stegemann, Christoph Böttcher, Pierangelo Metrangolo, Roland R. Netz, and Beate Koksch*

SUPPLEMENTARY INFORMATION

Content

1. Synthesis and Characterization of Fmoc-Tetrafluorinated Phenylalanine (^{1}H, ^{13}C and ^{19}F NMR spectra)

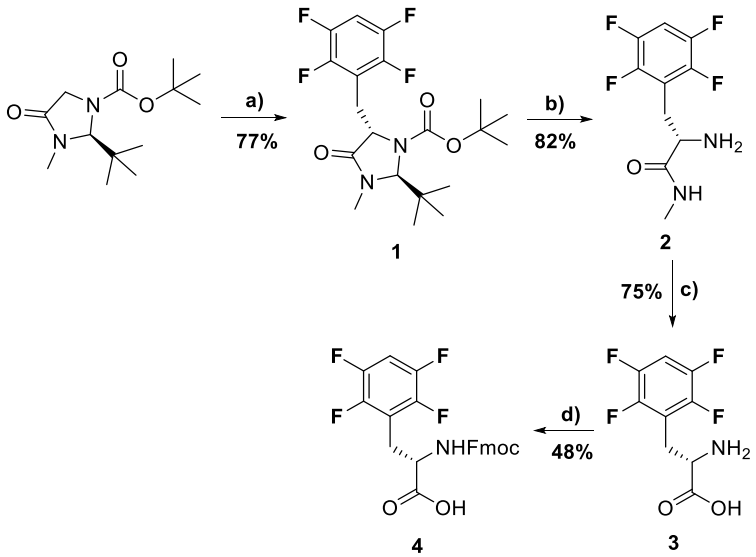

a) 2,3,5,6-tetrafluorobenzyl bromide, LDA, DMPU, -50°C; **b)** 1N HCl, reflux; **c)** 2N KOH, reflux; **d)** Fmoc-OSu, ACN, Na_2CO_3 (aq.)

Scheme S1: Synthetic scheme of Fmoc-**[2.3.5.6F]Phe**-OH **(4).**

A four-step synthesis for Fmoc-**[2.3.5.6F]Phe**-OH **(4)** is described in literature.[1] Published by Zheng *et al.* in 2009, this synthetic route starts with a stereoselective benzylation of Seebach's (*S*)-Boc-BMI by use of 2,3,4,5-tetrafluorobenzyl bromide. Followed by acid and subsequent base hydrolysis of intermediates in order to obtain H_2N-**[2.3.5.6F]Phe**-OH **(3)**, the desired compound **4** is formed through standard Fmoc-protection **[Scheme 1]**.

^{1}H, ^{13}C and ^{19}F NMR spectra of **1**-**4** are identical to the spectra reported by Zheng *et al.* and presented to confirm successful synthesis of all compounds.

1.1 Tert-butyl (2*S*,5*S*)-2-(tert-butyl)-3-methyl-4-oxo-5-(2,3,5,6 tetrafluorobenzyl)-imidazolidine-1-carboxylate (1)

DIPA (0.4 mL, 2.92 mmol) was dissolved in dry THF (1.5 mL) and chilled to -50 °C under argon protection, to which *n*-BuLi (2.5 N solution in hexane, 1.17 mL, 2.92 mmol) was added to give a fresh solution of LDA. After 15 min of stirring, DMPU (0.7 mL 5.85 mmol) and (*S*)-Boc-BMI **(14)** (500 mg, 1.95 mmol) in dry THF (2 mL) were added, and the mixture was kept stirring for additional 30 min at -50 °C. Then 2,3,5,6-tetrafluorobenzyl bromide (0.53 mL, 3.9 mmol) in dry THF (1 mL) was added. The reaction mixture was kept stirring at -50 °C for 3.5 h before it was quenched with saturated NH_4Cl solution (10 mL). After diluting the reaction mixture with H_2O (5 mL), the product was extracted with diethyl ether (4*20 mL). The organic layers were combined, washed with 2 N citric acid, sat.aq. $NaHCO_3$ and H_2O, and then dried over Na_2SO_4. The solvent was evaporated under reduced pressure and the crude product was purified by flash column chromatography (ethyl acetate/hexane, 1:5).

The title compound **1** was obtained as a white solid substance (628.7 mg, 1.50 mmol, 77%).

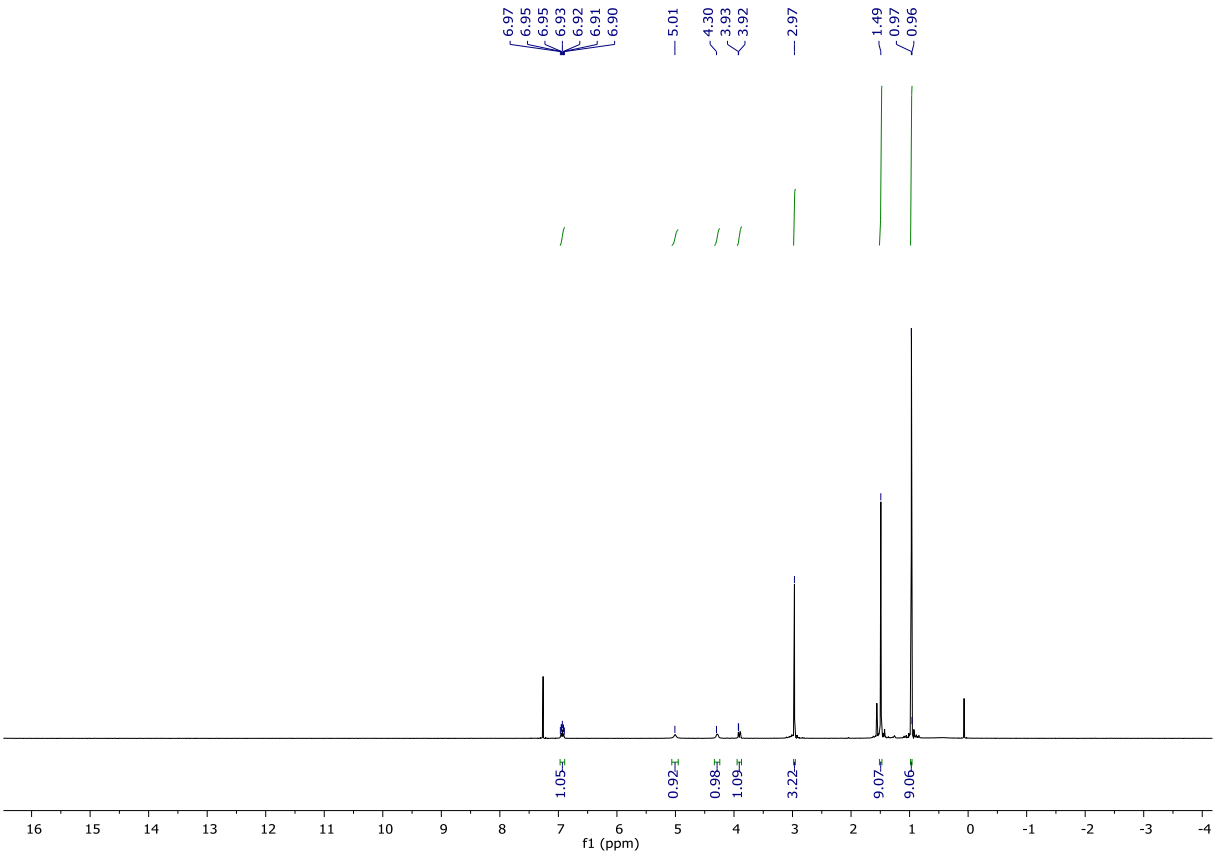

Figure S1: ^1H NMR (600 MHz, $CDCl_3$) of compound **1**.

^1H-NMR (500 MHz, $CDCl_3$): δ = 6.97 – 6.89 (m, 1H), 5.01 (s, 1H), 4.30 (s, 1H), 3.93 – 3.88 (m, 1H), 2.97 (s, 3H), 1.49 (s, 9H), 0.97 (s, 9H).

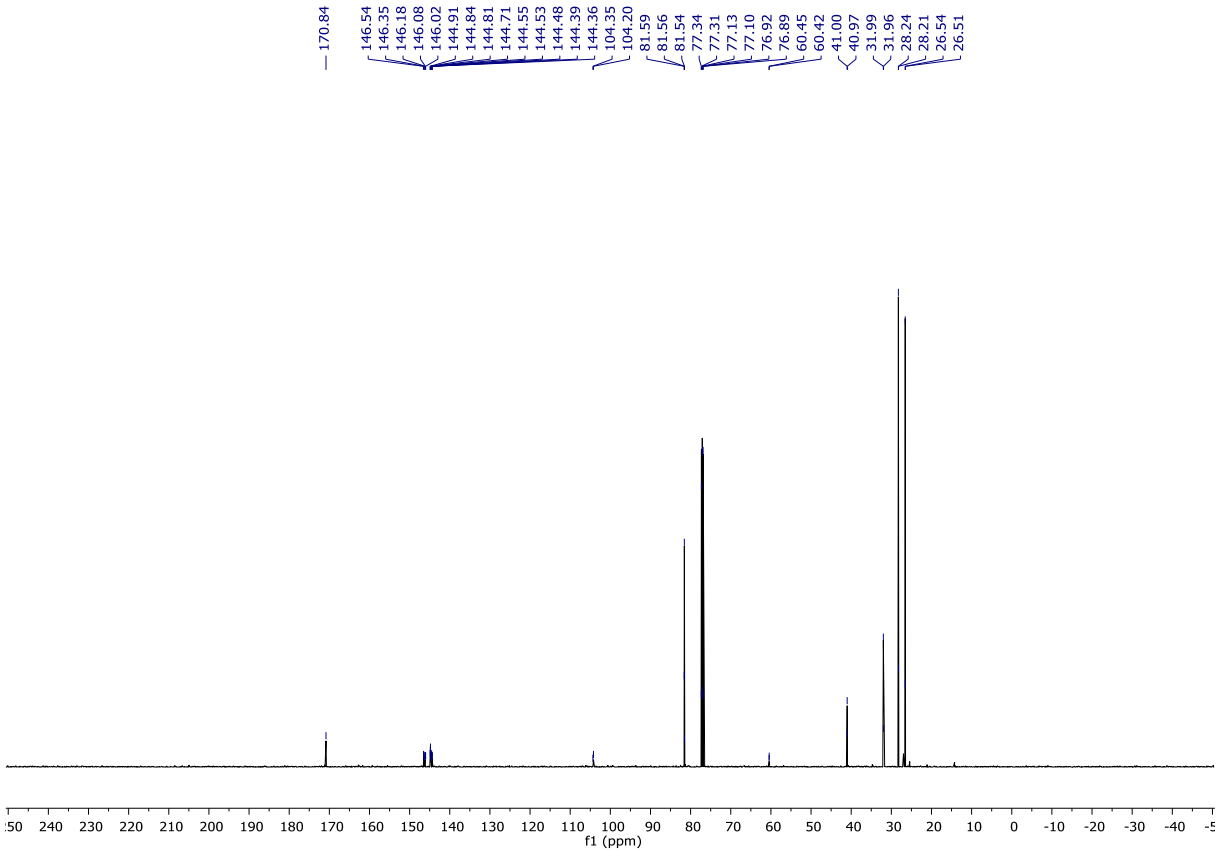

Figure S2: $^{13}C\{^{1}H\}$-NMR (151 MHz, $CDCl_3$) of compound **1**.

$^{13}C\{^{1}H\}$-NMR (151 MHz, $CDCl_3$): δ = 170.84, 146.44, 146.08, 104.34 , 104.18, 81.57, 60.44, 40.98, 31.97, 28.22, 26.54.

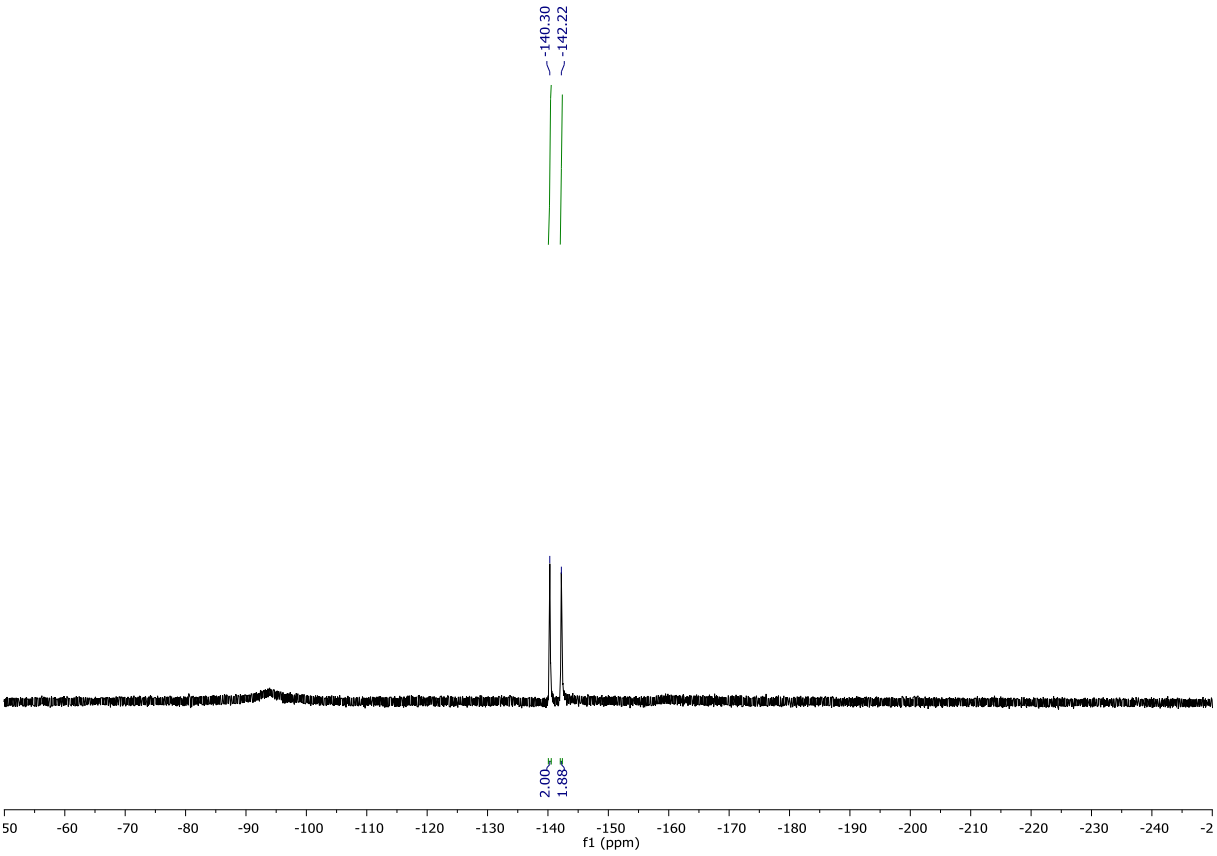

Figure S3: ^{19}F-NMR (471 MHz, $CDCl_3$) of compound **1**.

^{19}F-NMR (376 MHz, $CDCl_3$): δ = -140.18 – -140.47 (m, 2F), -142.09 – -142.36 (m, 2F).

1.2 (*S*)-2-Amino-N-methyl-3-(2,3,5,6-tetrafluorophenyl)-propanamide (2)

Compound **1** (628.7 mg, 1.50 mmol) was dissolved in methanol (20 mL) and mixed with 1 N HCl solution (13 mL) at rt. Afterwards the reaction mixture was kept refluxing (80 °C) overnight under argon protection. Then methanol was removed by evaporation and the pH of remaining aqueous phase was adjusted to 10 with 2 N KOH solution. Then the aqueous phase was extracted with DCM (10*20 mL). The combined organic phases were dried over Na_2SO_4, filtered, and the solvent was evaporated under reduced pressure. The crude product was purified by flash column chromatography (CH_2Cl_2/MeOH, 9:1, 2% DIPA).

The title compound **2** was obtained as a white solid substance (311.8 mg, 1.24 mmol, 82%).

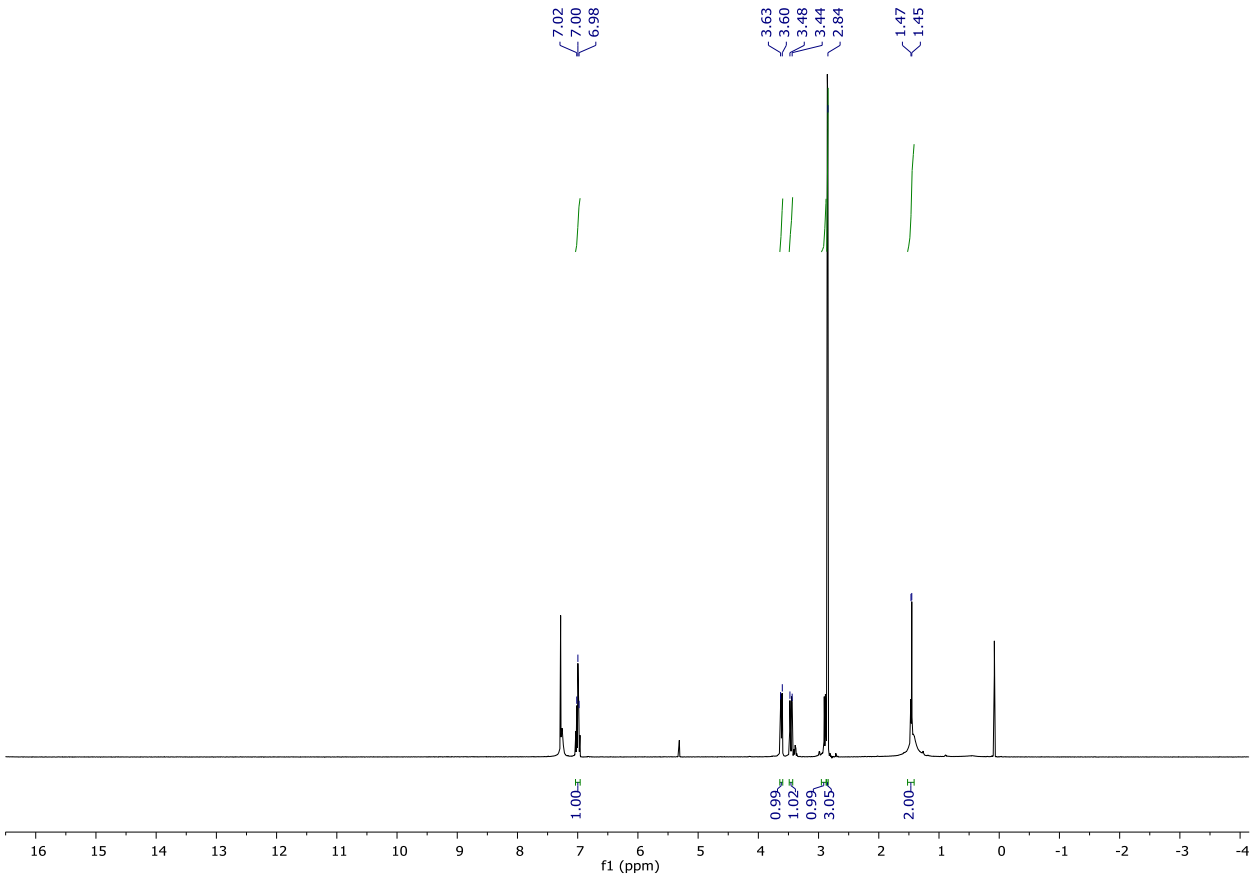

Figure S4: ^{1}H NMR (600 MHz, $CDCl_3$) of compound **2**.

^{1}H-NMR (400 MHz, $CDCl_3$): δ = 7.04 – 6.96 (m, 1H), 3.68 – 3.56 (m, 1H), 3.50 – 3.42 (m, 1H), 2.91 – 2.87 (m, 1H), 2.85 (d, J = 5.0 Hz, 3H), 1.49 – 1.44 (m, 2H).

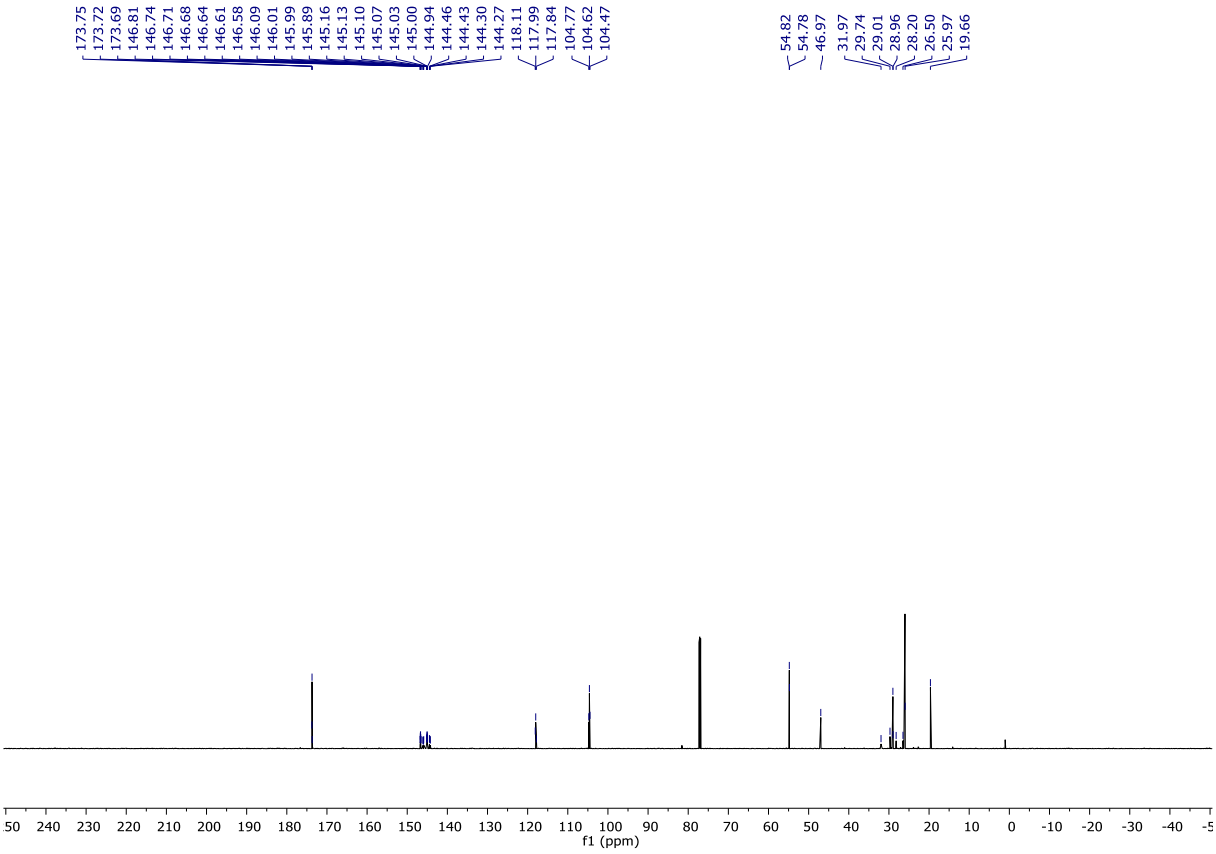

Figure S5: $^{13}C\{^{1}H\}$-NMR (151 MHz, $CDCl_3$) of compound **2**.

$^{13}C\{^{1}H\}$-NMR (151 MHz, $CDCl_3$): δ = 173.71, 146.32, 144.69, 117.97, 104.61, 54.77, 46.96, 29.00, 25.99, 19.68.

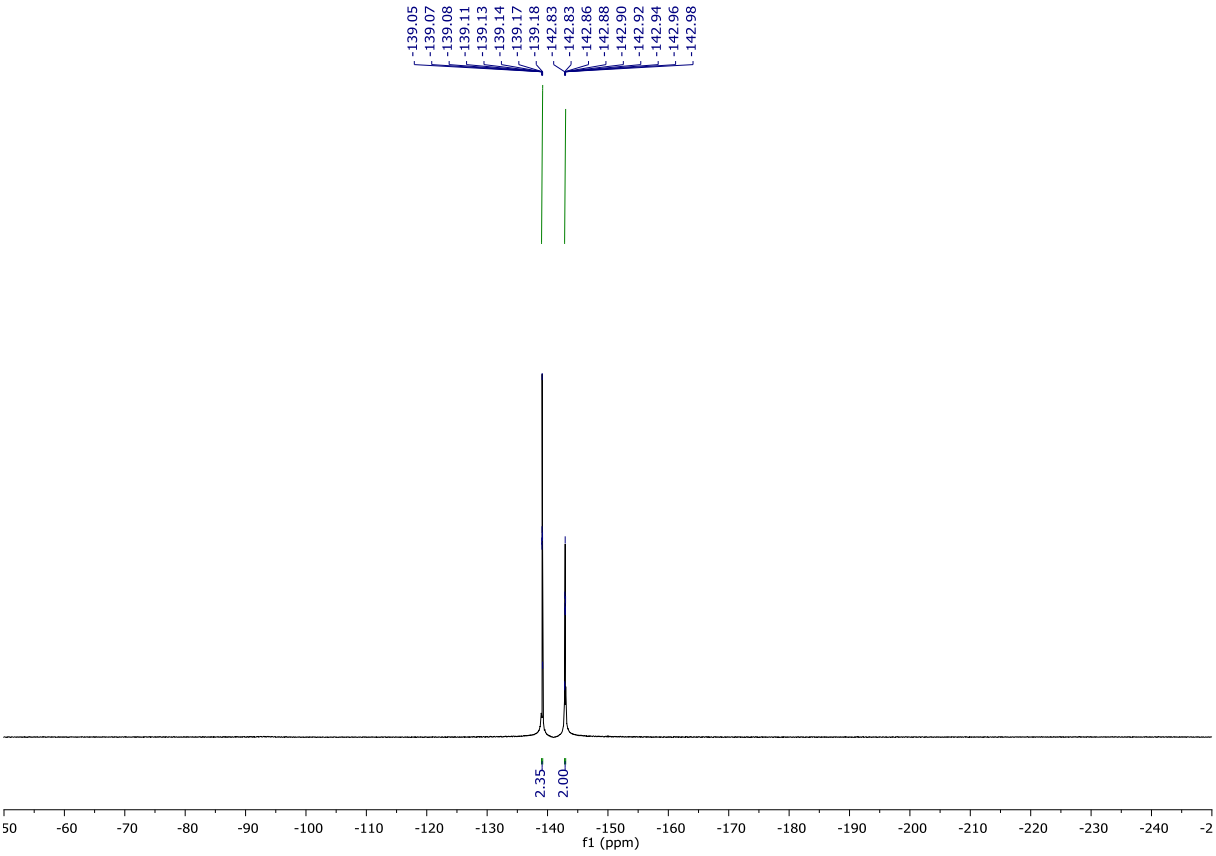

Figure S6: ^{19}F-NMR (376 MHz, $CDCl_3$) of compound **2**.

^{19}F-NMR (376 MHz, $CDCl_3$): δ = -139.01 – -139.20 (m, 2F), -142.78 – -143.03 (m, 2F).

1.3 (*S*)-2-amino-3-(2,3,5,6-tetrafluorophenyl)propanoic acid (3)

Compound **2** (311.8 mg, 1.24 mmol) was dissolved in 2 N KOH (20 mL) at rt, and then refluxed (100 °C) for 2.5 h. After adjusting the pH of the solution to 5 with 2 N HCl at rt, H_2O was removed *via* lyophilization. The residue was suspended in anhydrous ethanol (10 mL) and filtrated over a celite plug for separation of insoluble salt content. The supernatant was collected, and the solvent was evaporated *in vacuo*.

The title compound **3** was obtained as a white solid substance (220.5 mg, 0.93 mmol, 75%).

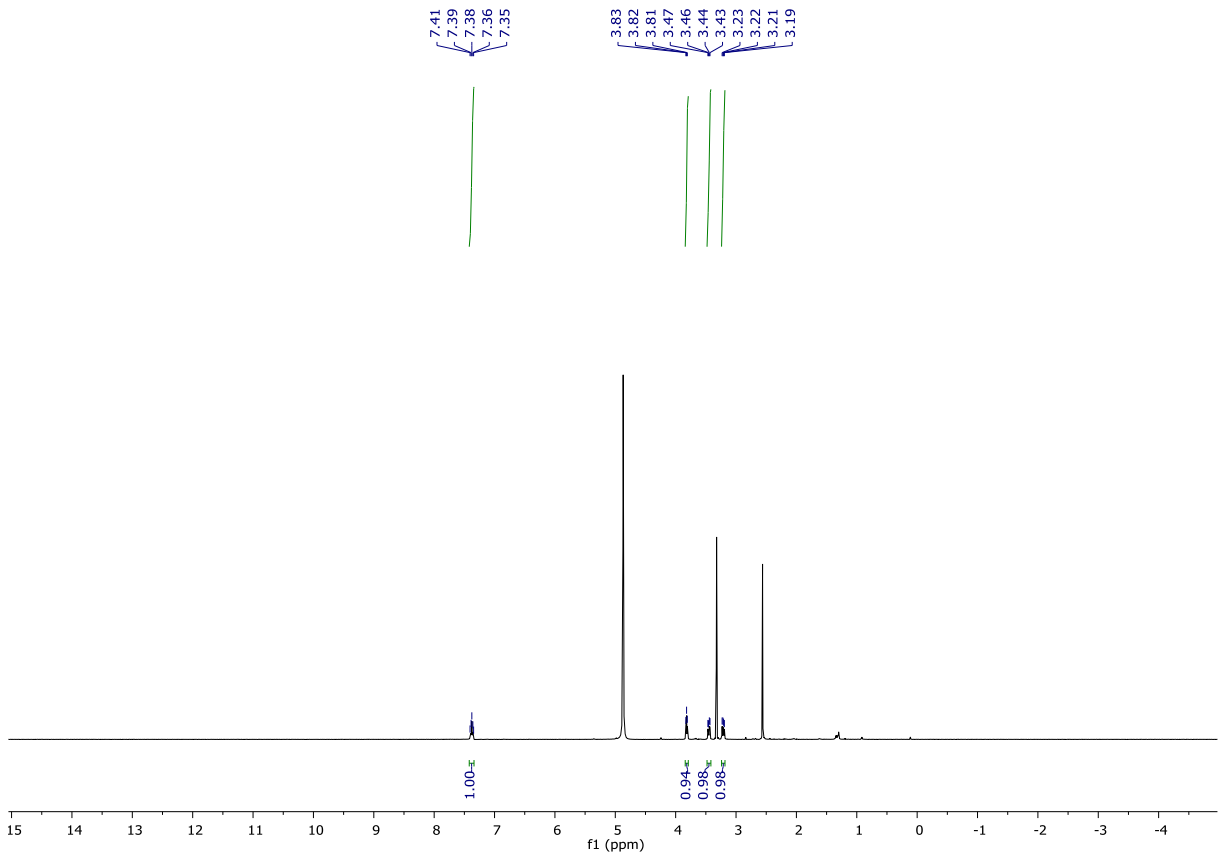

Figure S7: ^{1}H NMR (600 MHz, CD_3OD) of compound **3**.

^{1}H-NMR (600 MHz, CD_3OD): δ = 7.38 – 7.35 (m, 1H), 3.82 (t, J = 7.3 Hz, 1H), 3.47 – 3.43 (m, 1H), 3.23 – 3.19 (m, 1H).

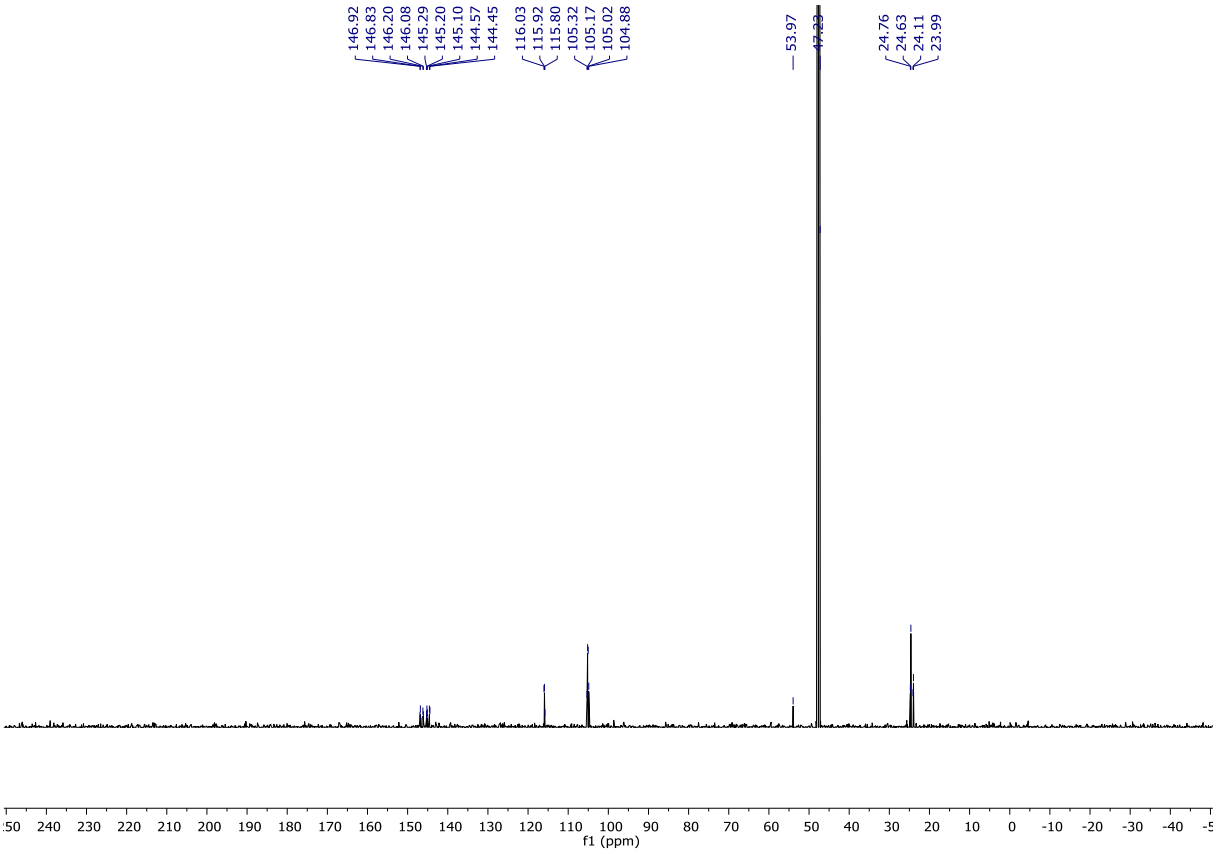

Figure S8: $^{13}C\{^{1}H\}$-NMR (151 MHz, CD_3OD) of compound **3**.

$^{13}C\{^{1}H\}$-NMR (151 MHz, CD_3OD): δ = 146.37, 144.88, 115.96, 105.07, 53.98, 24.62, 24.04.

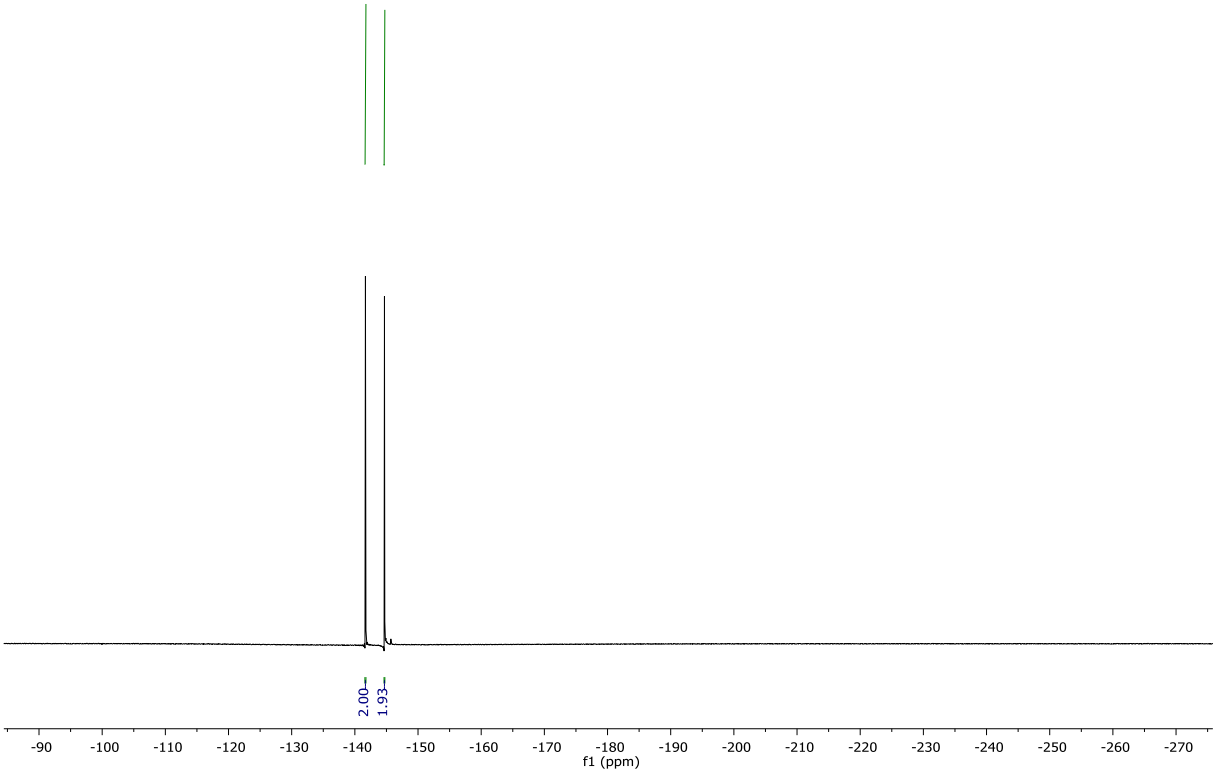

Figure S9: ^{19}F-NMR (376 MHz, CD_3OD) of compound **3**.

^{19}F-NMR (376 MHz, CD_3OD): δ = -141.56 – -141.75 (m, 2F), -144.59 – -144.77 (m, 2F).

1.4 (*S*)-2-((((9H-fluoren-9-yl)methoxy)carbonyl)amino)-3-(2,3,5,6-tetrafluorophenyl)Propanoic acid (4)

The amino acid **3** (165.9 mg, 0.69 mmol) was suspended in 5% $Na_2CO_{3aq.}$ (5 mL) at 0 °C. Afterwards a solution of Fmoc-OSu (282.9 mg, 0.83 mmol) in ACN (5 mL) was added dropwise and the reaction mixture was stirred for 2 h while warming up to room temperature. Then H_2O (20 mL) was added and the diluted mixture was acidified to pH ~ 2 with HCl_{conc}. The aqueous phase was extracted with ethyl acetate (6*30 mL). The combined organic phases were over Na_2SO_4, filtered, and concentrated *in vacuo*. Finally, the crude product was purified by column chromatography with ethyl acetate/*n*-hexane, 1:1 to elute unreacted Fmoc-OSu, followed by ethyl acetate/*n*-hexane, 1:1, 2% acetic acid to yield Fmoc-**[2.3.5.6F]Phe**-OH.

The title compound **4** was obtained as a white solid substance (153.9 mg, 0.33 mmol, 48%).

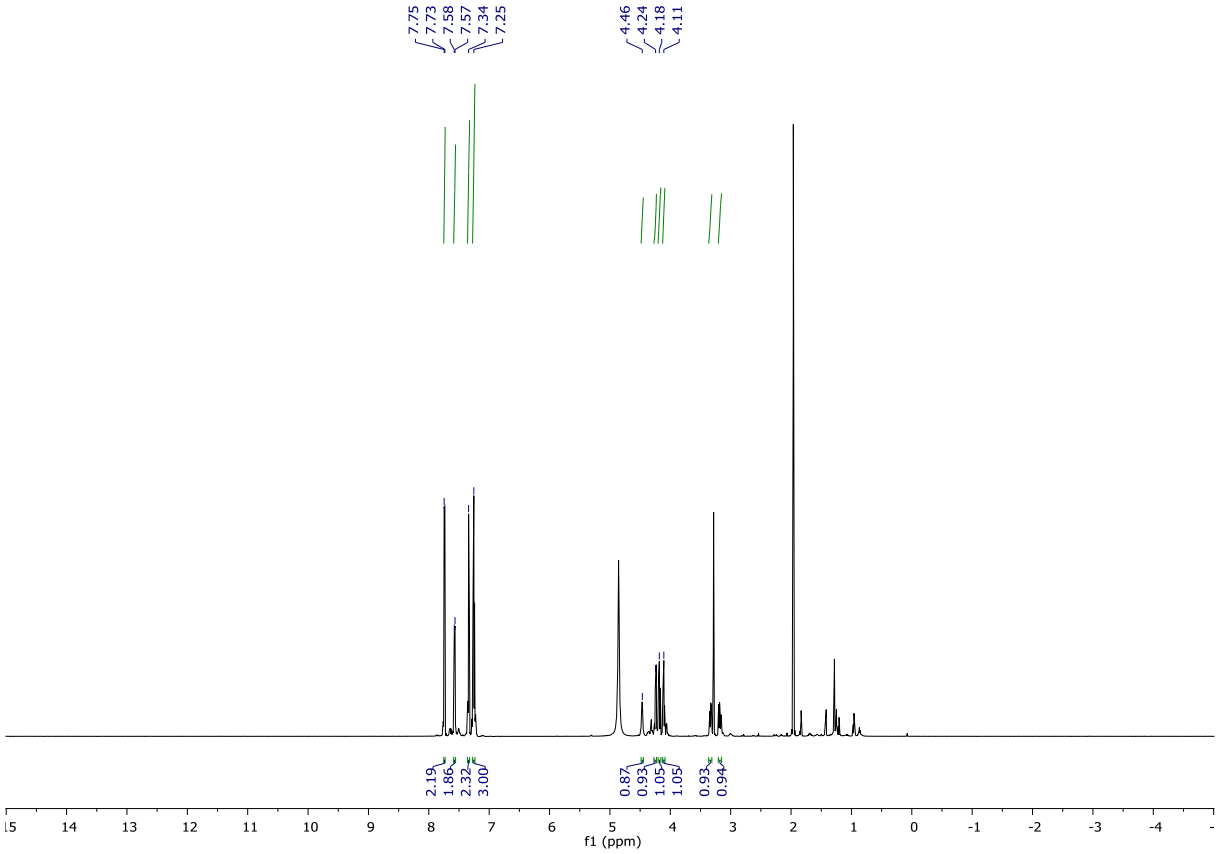

Figure S10: ^{1}H-NMR (600 MHz, CD_3OD) of compound **4**.

^{1}H-NMR (600 MHz, CD_3OD): δ = 7.72 (d, J = 7.6 Hz, 2H), 7.56 (d, J = 8.6 Hz, 2H), 7.33 (t, J = 7.5 Hz, 2H), 7.24 (d, J = 11.7 Hz, 3H), 4.49 – 4.45 (m, 1H), 4.26 – 4.21 (m, 1H), 4.19 – 4.14 (m, 1H), 4.11 – 4.07 (m, 1H), 3.36 – 3.30 (m, 1H), 3.21 – 3.14 (m, 1H).

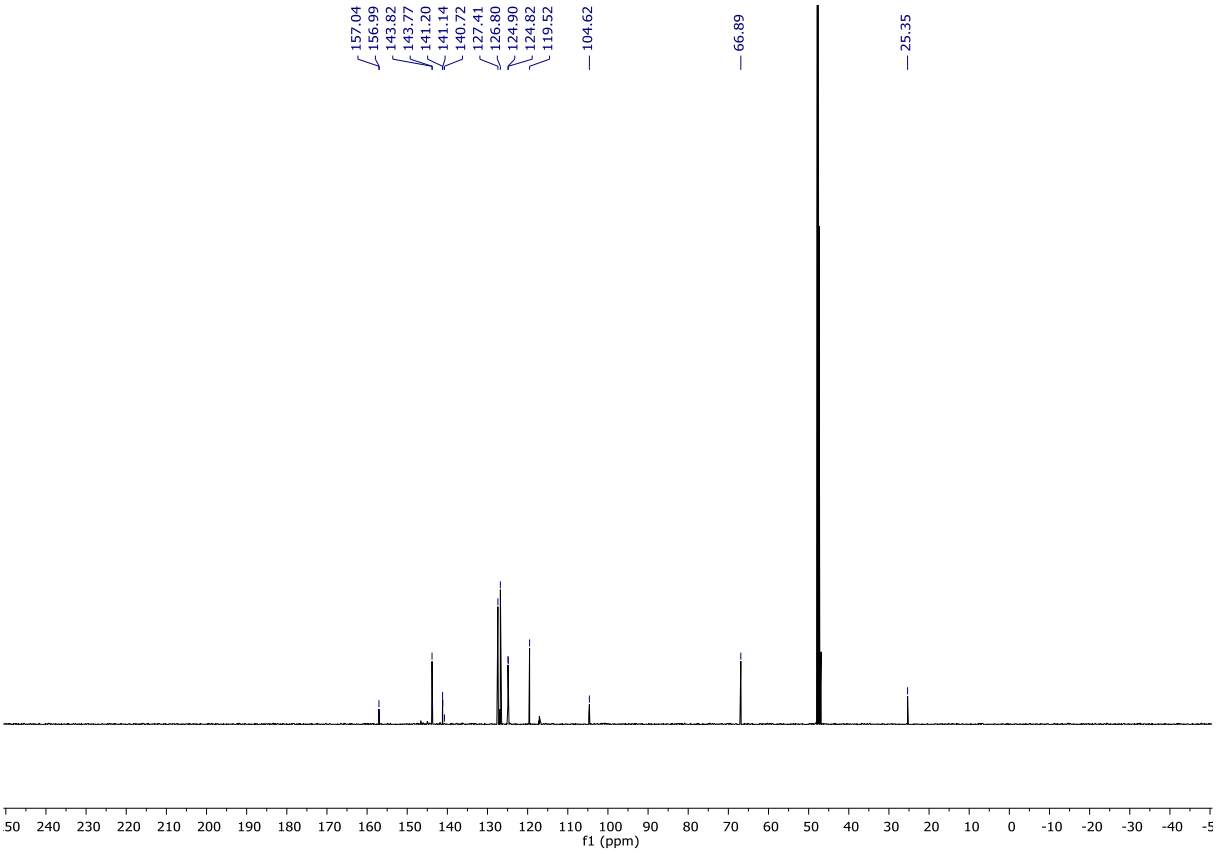

Figure S11: $^{13}C\{^{1}H\}$-NMR (151 MHz, CD_3OD) of compound **4**.

$^{13}C\{^{1}H\}$-NMR (151 MHz, CD_3OD): δ = 157.01, 143.78, 141.15, 127.42, 126.73, 124.89, 119.54, 104.65, 66.86, 25.35.

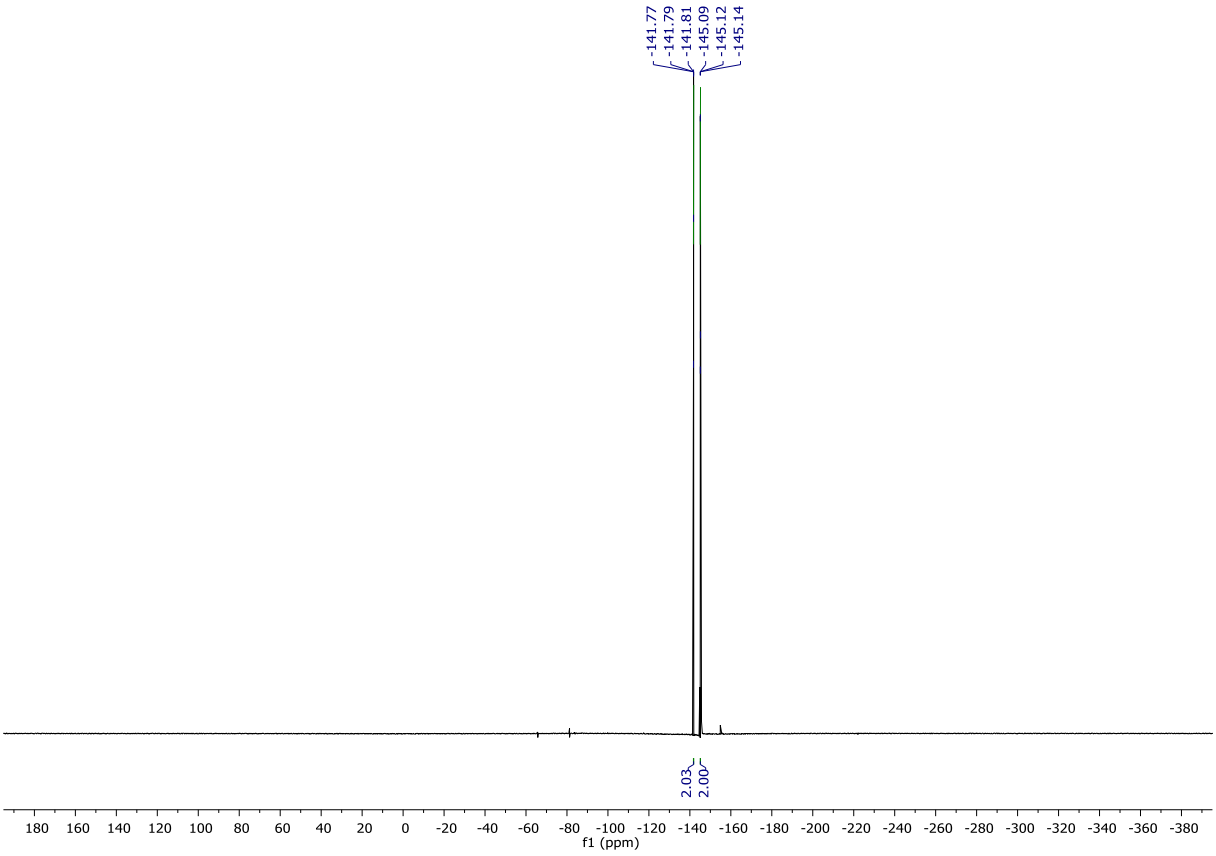

Figure S12: ^{19}F-NMR (471 MHz, CD_3OD) of compound **4**.

^{19}F-NMR (471 MHz, CD_3OD): δ = -141.71 – -141.96 (m, 2F), -145.07 – -145.20 (m, 2F).

2. Synthesized NFGAIL Sequences

The peptides NFGAIL, N-**[3.5F]Phe**-GAIL, N-**[2.3.5.6F]Phe**-GAIL, N-**[2.3.4.5.6F]Phe**-GAIL and N-**[2.3.5.6F][4I]Phe**-GAIL were prepared by manual solid phase peptide synthesis according to Fmoc-strategy. Purification and subsequent characterization were carried out by analytical/semi-preparative HPLC and ESI-ToF mass spectrometry.

2.1 Solid Phase Peptide Synthesis - NFGAIL

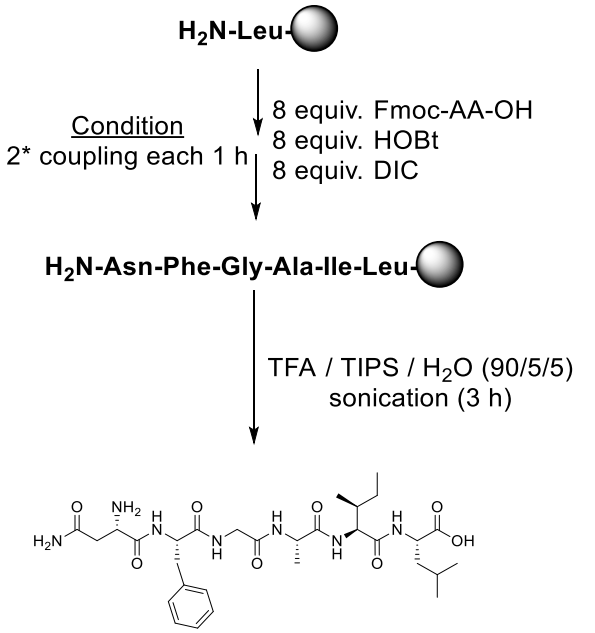

Analytical HPLC - NFGAIL

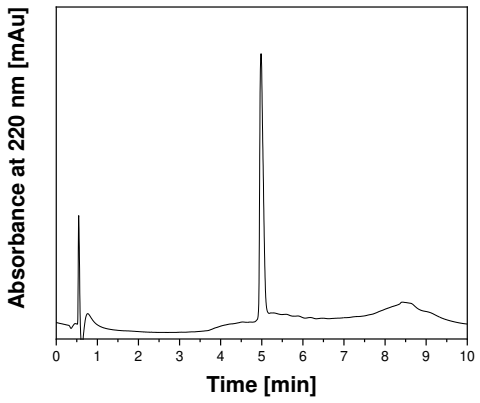

Retention Time[t_R]	
Analytical HPLC:	4.983 min

Figure S13: Analytical HPLC chromatograms of purified peptide NFGAIL; column: Purospher®STAR RP-C18 endcapped (2 µM, 50 x 2.1 mm }; Solvent A was H20 , solvent B was acetonitrile, both containing 0.1 % (v/v) TFA; linear gradient from 5–70% ACN + 0.1% TFA within 10 min.

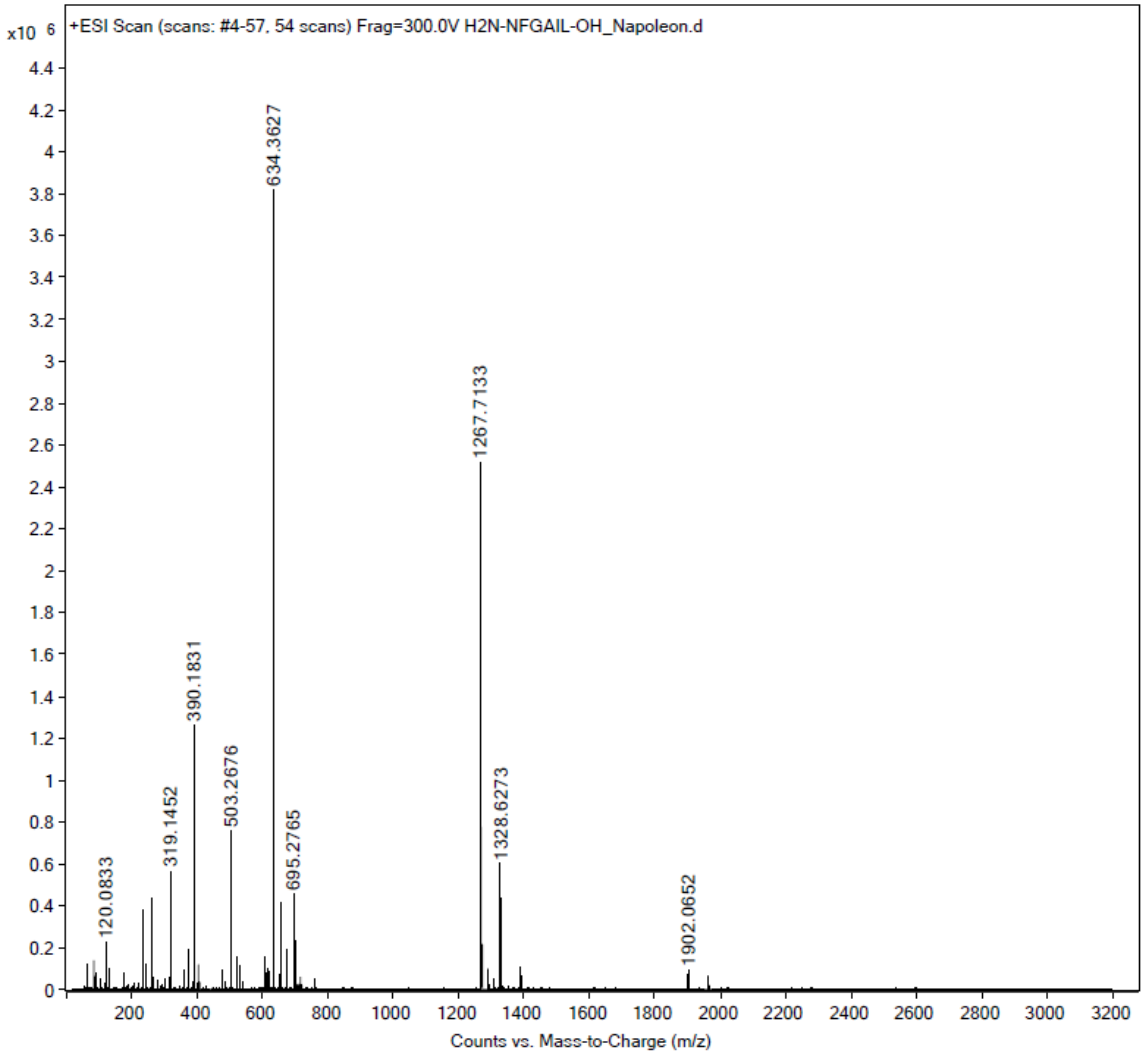

Figure S14: High resolution mass spectrometry (HRMS) – NFGAIL.

ESI-HRMS (m/z)	Calculated Mass	Observed Mass
$[M+H]^+$	634.3564	634.3627
$[M+2H]^+$	635.3642	635.3656
$[M+3H]^+$	636.3720	636.3680

2.2 Solid Phase Peptide Synthesis - N-[4F]Phe-GAIL

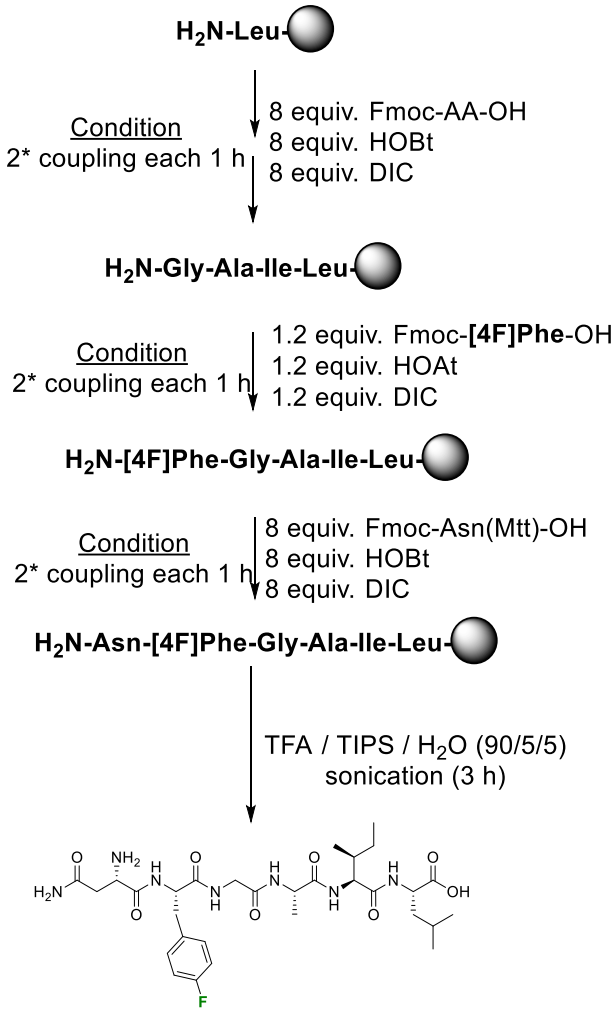

Analytical HPLC - N-[4F]Phe-GAIL

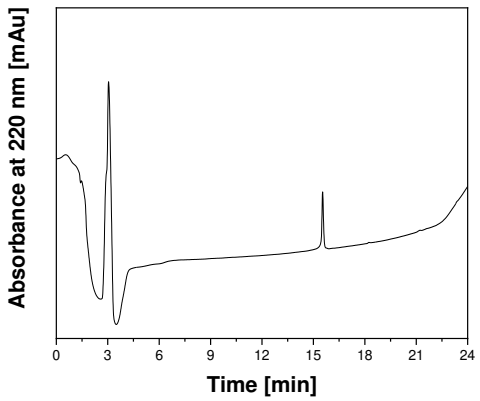

Figure S15: Analytical HPLC chromatograms of purified peptide N-**[4F]Phe**-GAIL; column: Purospher®STAR RP-C18 endcapped (2 µM, 50 x 2.1 mm }; Solvent A was H20 , solvent B was acetonitrile, both containing 0.1 % (v/v) TFA; linear gradient from 5–100% ACN + 0.1% TFA within 18 min.

Retention Times[t_R]	
Analytical HPLC:	15.540 min

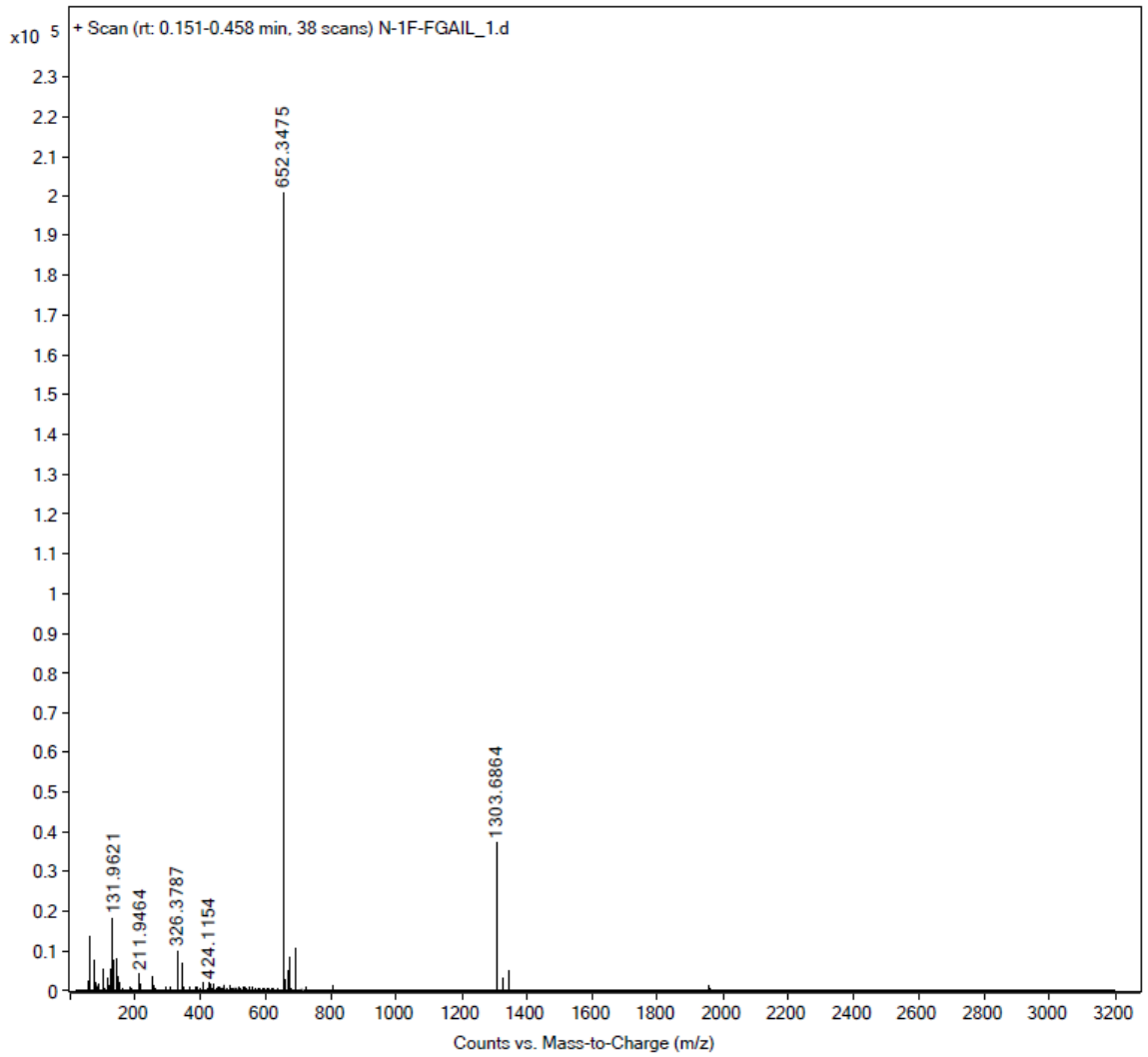

Figure S16: High resolution mass spectrometry (HRMS) – N-**[4F]Phe**-GAIL.

ESI-HRMS (m/z)	Calculated Mass	Observed Mass
$[M+H]^+$	652.3470	652.3475
$[M+2H]^+$	653.3548	653.3500
$[M+3H]^+$	654.3626	654.3522

2.3 Solid Phase Peptide Synthesis - N-[3.5F]Phe-GAIL

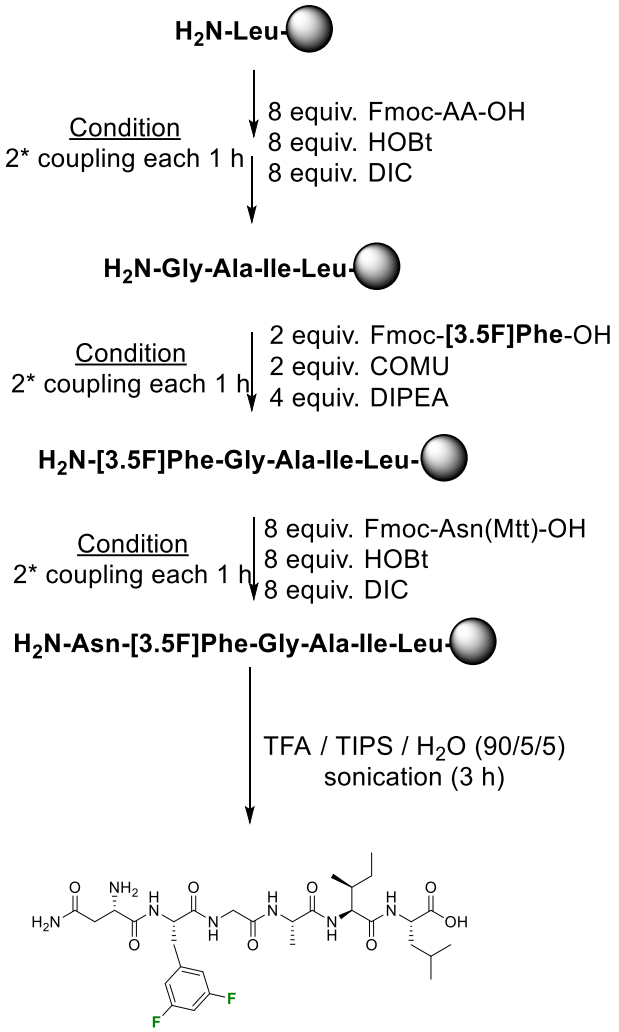

Analytical HPLC - N-[3.5F]Phe-GAIL

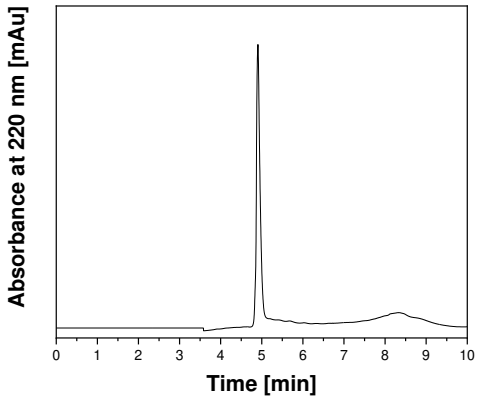

Figure S17: Analytical HPLC chromatograms of purified peptide N-**[3.5F]Phe**-GAIL; column: Purospher®STAR RP-C18 endcapped (2 µM, 50 x 2.1 mm }; Solvent A was H20 , solvent B was acetonitrile, both containing 0.1 % (v/v) TFA; linear gradient from 5–70% ACN + 0.1% TFA within 10 min.

Retention Times[t_R]	
Analytical HPLC:	4.907 min

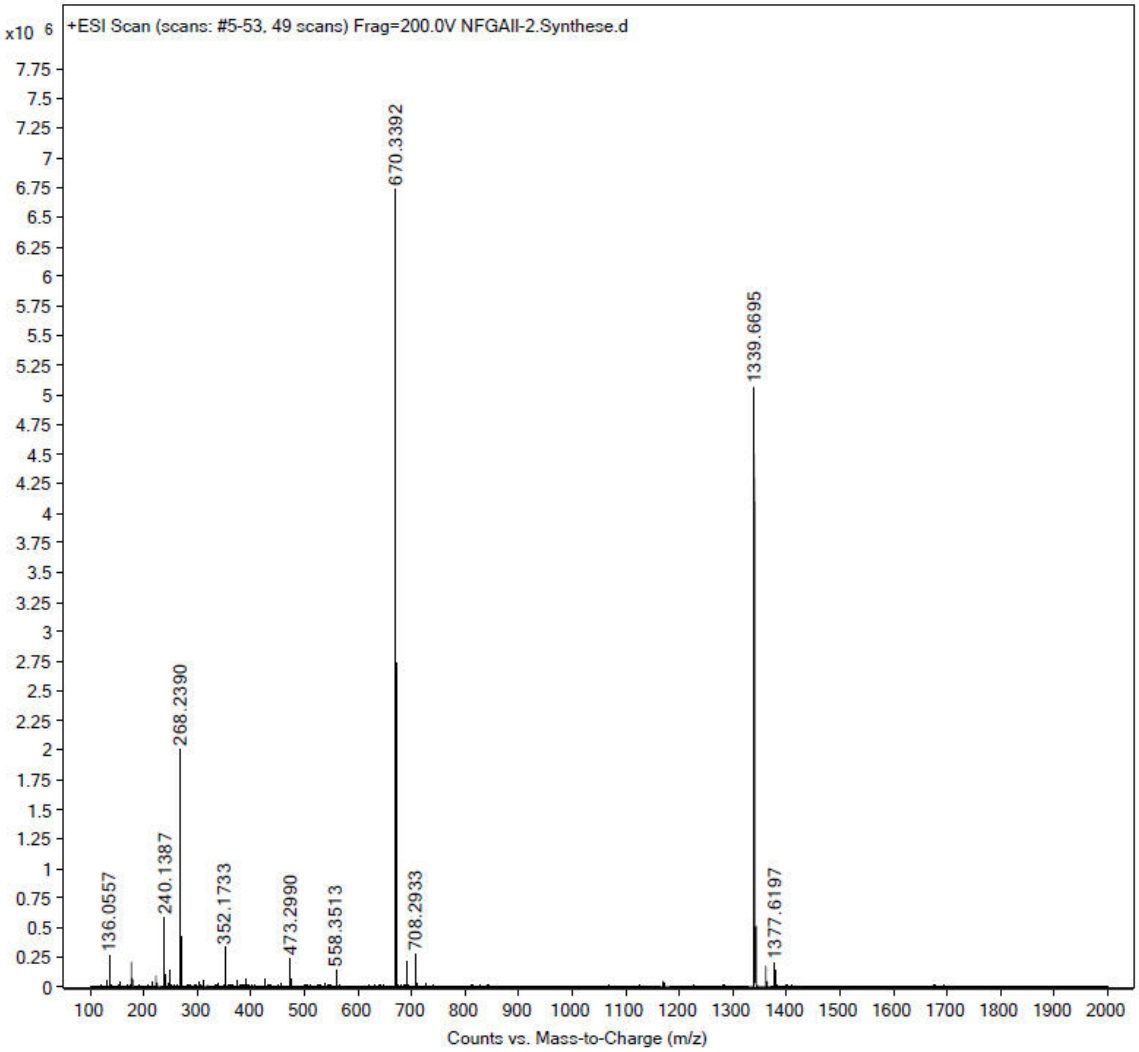

Figure S18: High resolution mass spectrometry (HRMS) - N-**[3.5F]Phe**-GAIL.

ESI-HRMS (m/z)	Calculated Mass	Observed Mass
$[M+H]^+$	670.3375	670.3392
$[M+2H]^+$	671.3454	671.3416
$[M+3H]^+$	672.3532	672.3444

2.4 Solid Phase Peptide Synthesis - N-[2.3.5.6F]Phe-GAIL

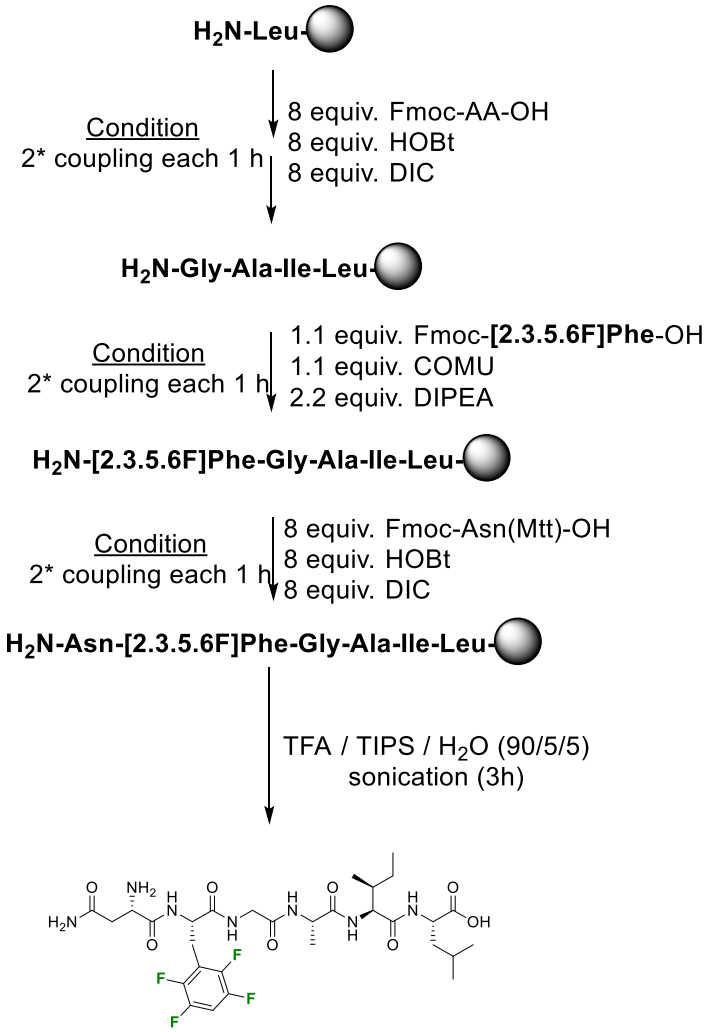

Analytical HPLC - N-[2.3.5.6F]Phe-GAIL

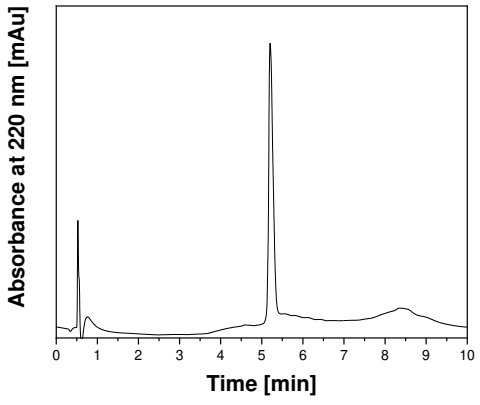

Figure S19: Analytical HPLC chromatograms of purified peptide N-**[2.3.5.6F]Phe**-GAIL; column: Purospher®STAR RP-C18 endcapped (2 µM, 50 x 2.1 mm }; Solvent A was H20 , solvent B was acetonitrile, both containing 0.1 % (v/v) TFA; linear gradient from 5–70% ACN + 0.1% TFA within 10 min.

Retention Times[t_R]	
Analytical HPLC:	5.203 min

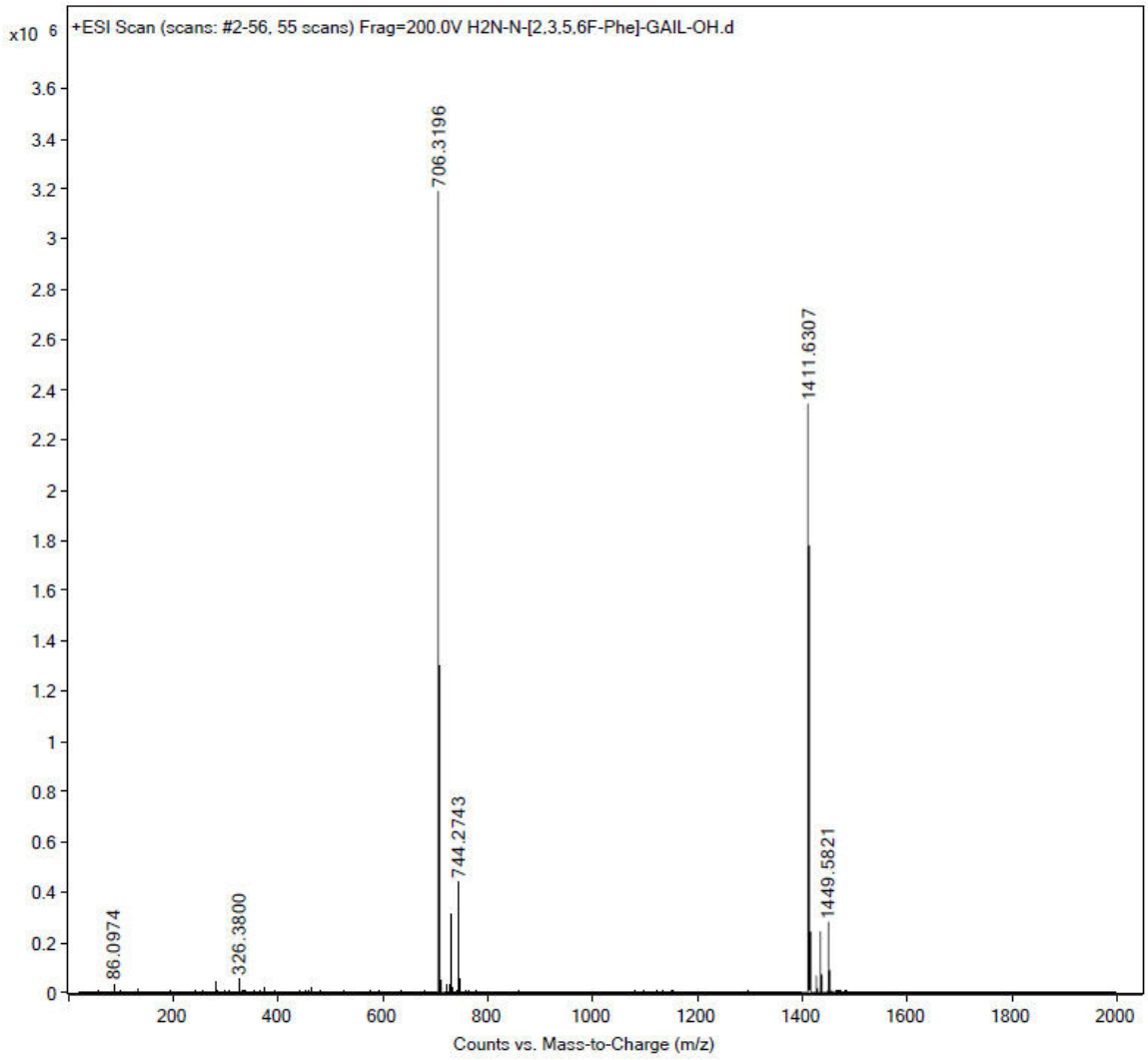

Figure S20: High resolution mass spectrometry (HRMS) - N-**[2.3.5.6F]Phe**-GAIL.

ESI-HRMS (m/z)	Calculated Mass	Observed Mass
$[M+H]^+$	706.3187	706.3196
$[M+2H]^+$	707.3265	707.3227
$[M+3H]^+$	708.3344	708.3247

2.5 Solid Phase Peptide Synthesis - N-[2.3.4.5.6F]Phe-GAIL

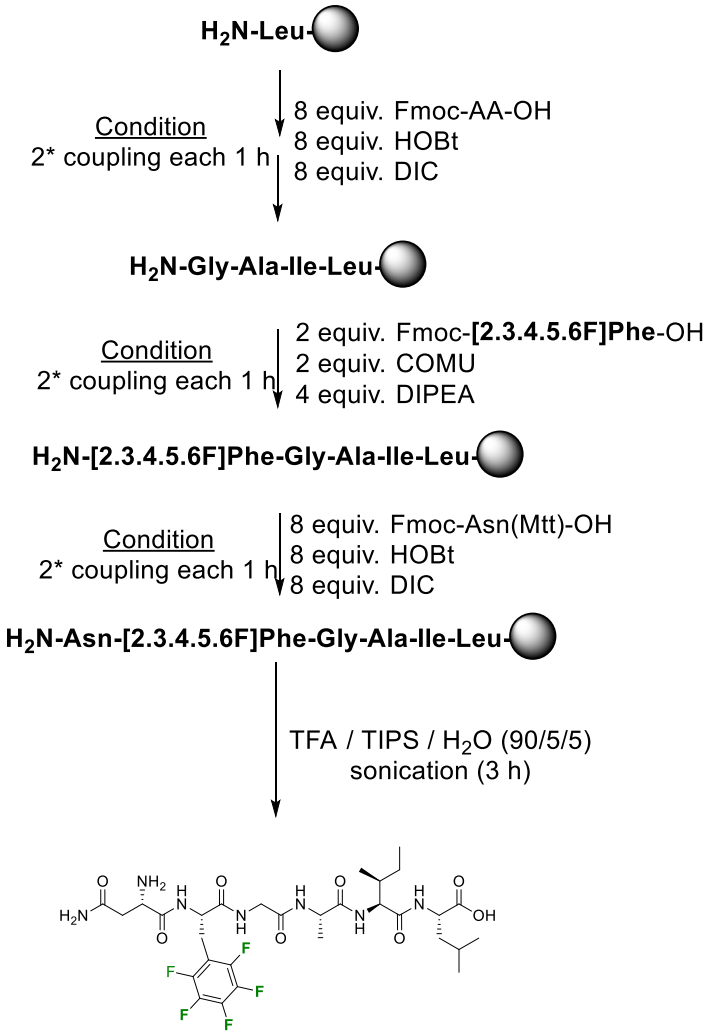

Analytical HPLC - N-[2.3.4.5.6F]Phe-GAIL

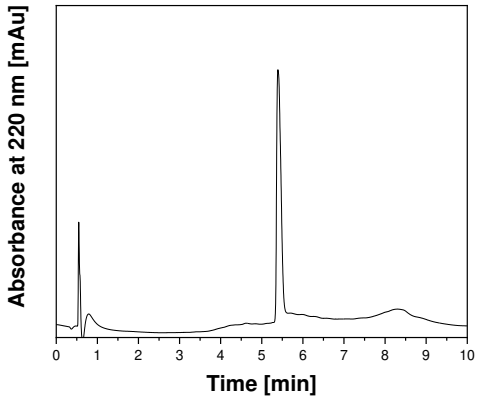

Retention Times[t_R]	
Analytical HPLC:	5.393 min

Figure S21: Analytical HPLC chromatograms of purified peptide N-**[2.3.4.5.6F]Phe**-GAIL; column: Purospher®STAR RP-C18 endcapped (2 µM, 50 x 2.1 mm }; Solvent A was H20 , solvent B was acetonitrile, both containing 0.1 % (v/v) TFA; linear gradient from 5–70% ACN + 0.1% TFA within 10 min.

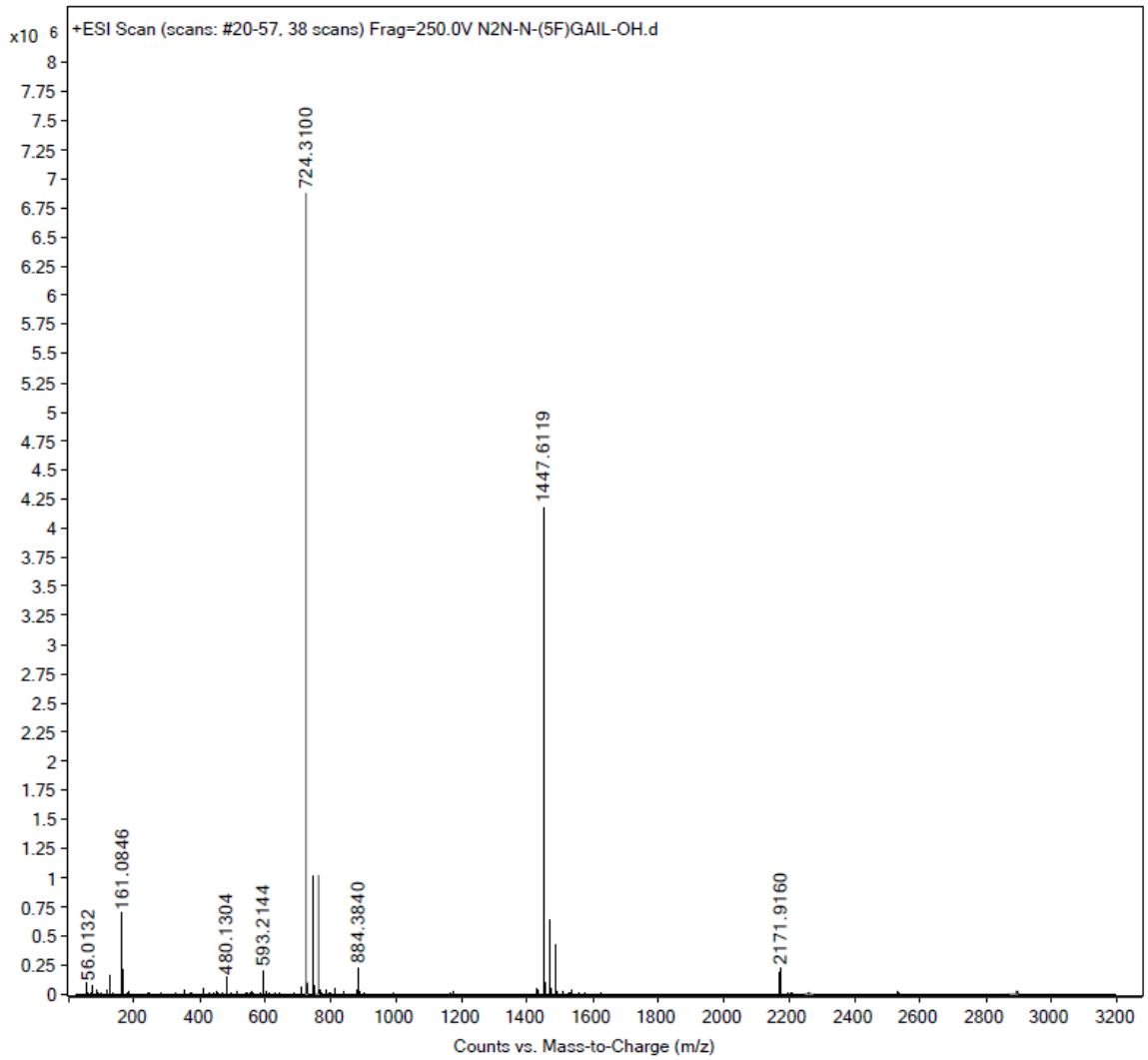

Figure S22: High resolution mass spectrometry (HRMS) - N-**[2.3.4.5.6F]Phe**-GAIL.

ESI-HRMS (m/z)	Calculated Mass	Observed Mass
$[M+H]^+$	724.3093	724.3100
$[M+2H]^+$	725.3171	725.3126
$[M+3H]^+$	726.3249	726.3154

2.6 Solid Phase Peptide Synthesis - N-[2.3.5.6F][4I]Phe-GAIL

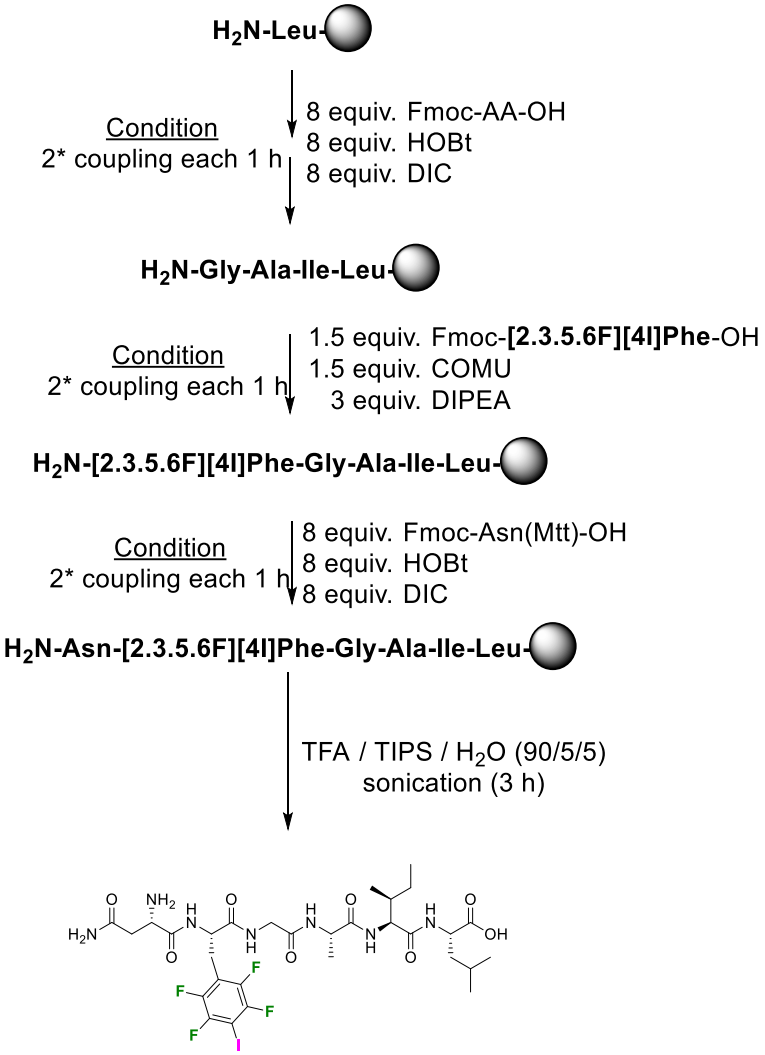

Analytical HPLC - N-[2.3.5.6F][4I]Phe-GAIL

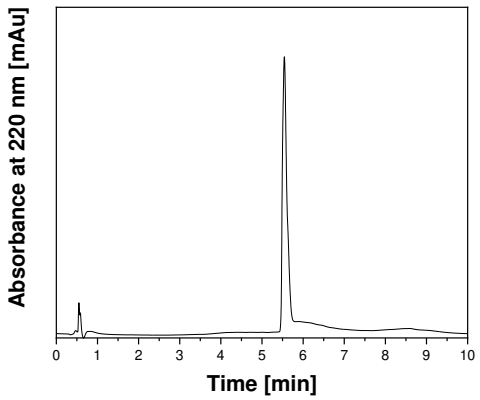

Figure S23: Analytical HPLC chromatograms of purified peptide N-**[2.3.5.6F][4I]Phe**-GAIL; column: Purospher®STAR RP-C18 endcapped (2 µM, 50 x 2.1 mm }; Solvent A was H20 , solvent B was acetonitrile, both containing 0.1 % (v/v) TFA; linear gradient from 5–70% ACN + 0.1% TFA within 10 min.

Retention Times[t_R]	
Analytical HPLC:	5.570 min

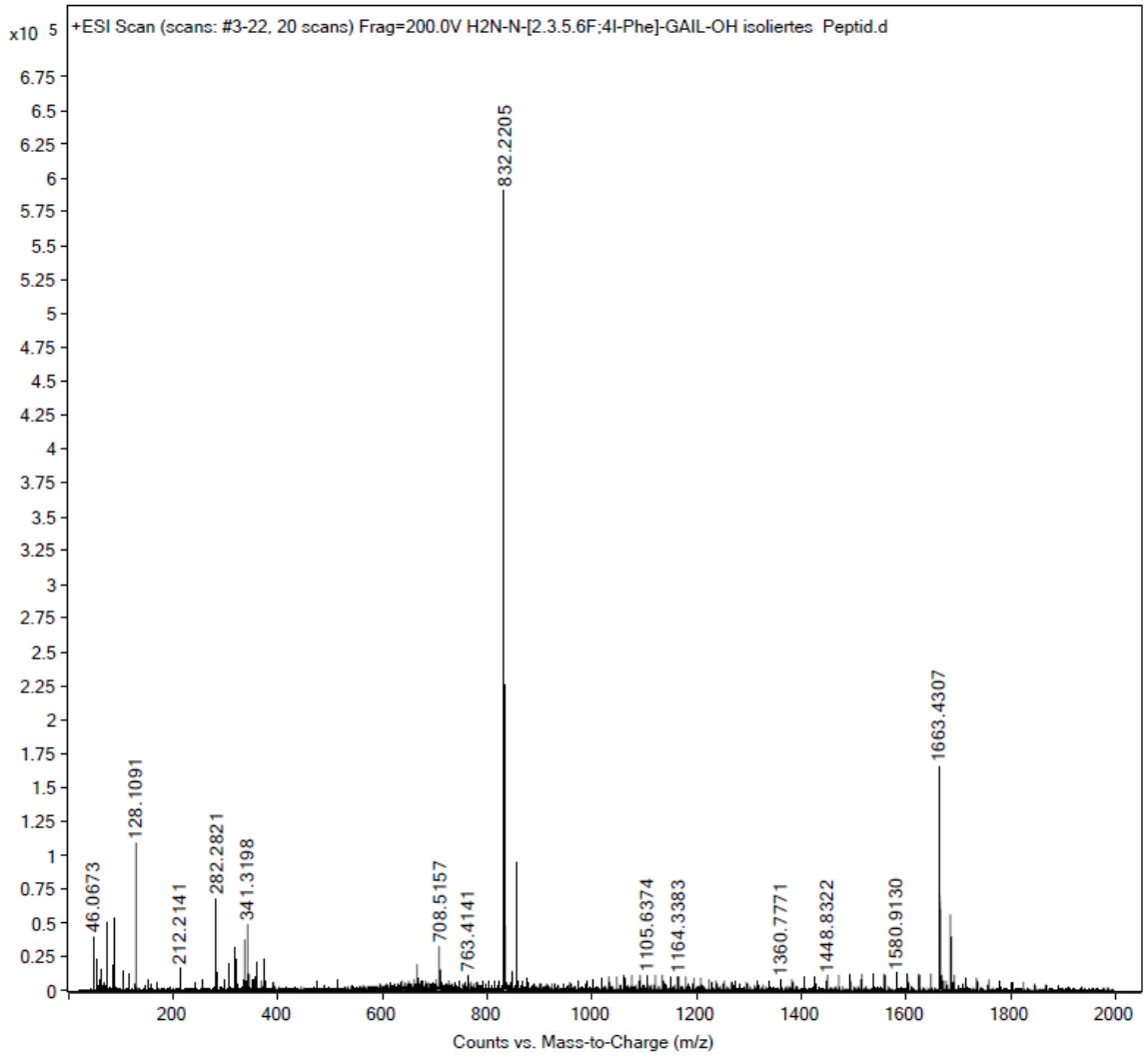

Figure S24: High resolution mass spectrometry (HRMS) - N-**[2.3.5.6F][4I]Phe**-GAIL.

ESI-HRMS (m/z)	Calculated Mass	Observed Mass
$[M+H]^+$	832.2154	832.2205
$[M+2H]^+$	833.2232	833.2232
$[M+3H]^+$	834.2310	834.2250

3. Thioflavin T Fluorescence Assay for Amyloid Fibril Detection

In this chapter, two further nearly congruent curves obtained from independently prepared samples of all halogenated NFGAIL variants are presented, emphasizing reproducibility of aggregation behavior. Furthermore, all used concentrations for the investigation of NFGAIL amyloid self-assembly kinetics are listed in **Table S1.**

Table S1: Lag times of halogenated NFGAIL variants determined *via* ThT fluorescence staining.

Peptide	Concentration	Lag Time
N-**[4F]Phe**-GAIL	4 mM	6.3 h
	3 mM	**- [a] -**
N-**[3.5F]Phe**-GAIL	4 mM	17.6 – 19.5 h
	3 mM	**- [b] -**
N-**[2.3.5.6F]Phe**-GAIL	4 mM	1.0 – 2.5 h
	3 mM	8.3 – 8.6 h
	1.5 mM	**- [b] -**
N-**[2.3.4.5.6F]Phe**-GAIL	4 mM	**- [c] -**
	3 mM	0.3 h
	1.5 mM	**- [b] -**
N-**[2.3.5.6F][4I]Phe**-GAIL	4 mM	**- [c] -**
	3 mM	**- [c] -**
	2.5 mM	**- [c] -**
	1 mM	3.8 h – 4.1 h

[a] Aggregation was not detected after a period of 20 h.
[b] Aggregation was not detected after a period of 40 h.
[c] Immediately detected aggregation after preparation of sample.

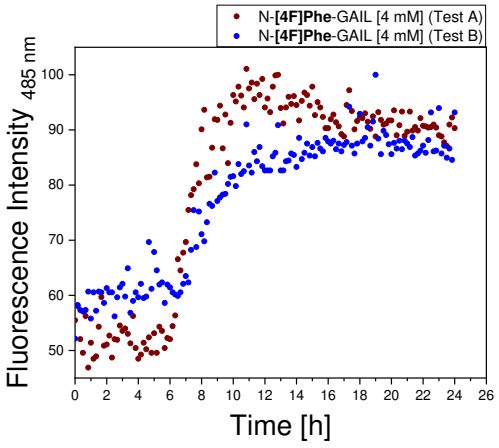

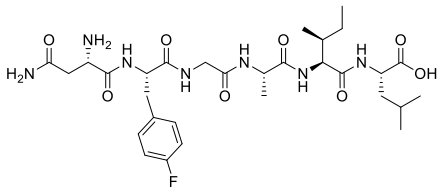

Figure S25: Two individual (brown and blue symbols) Thioflavin T assays of an incubated N-**[4F]Phe**-GAIL (4 mM) sample in ammonium acetate (10 mM) buffer.

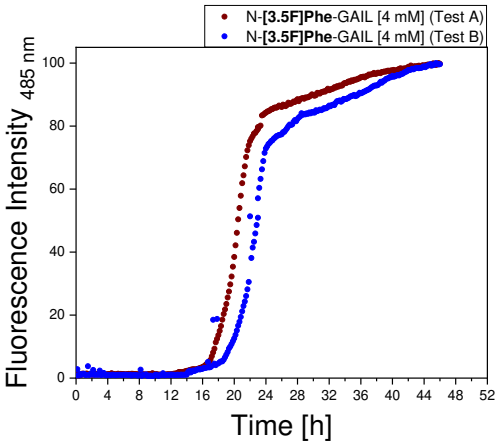

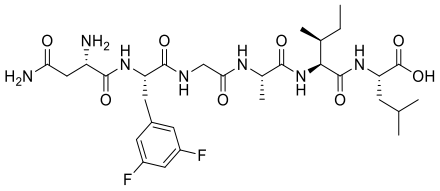

Figure S26: Two individual (brown and blue symbols) Thioflavin T assays of an incubated N-**[3.5F]Phe**-GAIL (4 mM) sample in ammonium acetate (10 mM) buffer.

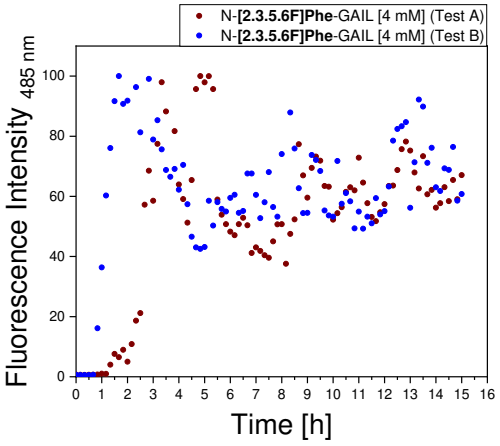

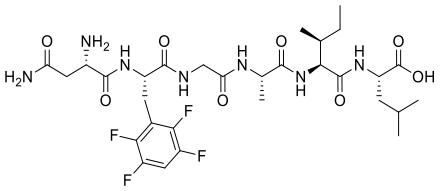

Figure S27: Two individual (brown and blue symbols) Thioflavin T assays of an incubated N-**[2.3.5.6F]Phe**-GAIL (4 mM) sample in ammonium acetate (10 mM) buffer.

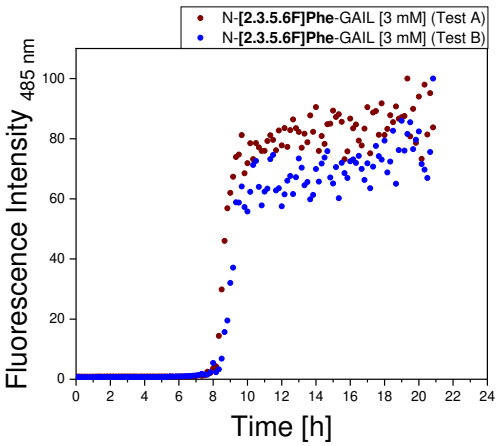

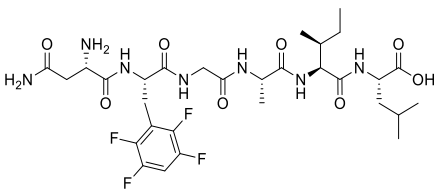

Figure S28: Two individual (brown and blue symbols) Thioflavin T assays of an incubated N-**[2.3.5.6F]Phe**-GAIL (3 mM) sample in ammonium acetate (10 mM) buffer.

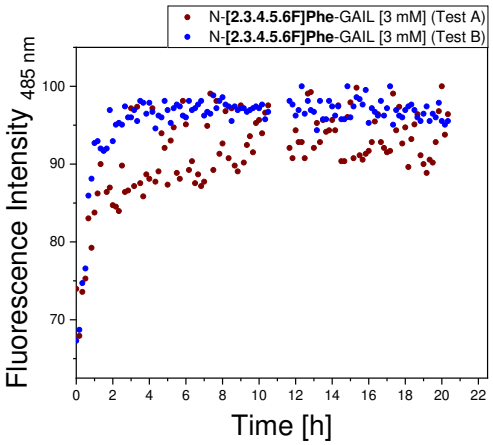

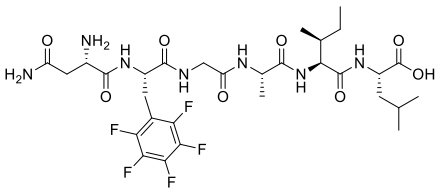

Figure S29: Two individual (brown and blue symbols) Thioflavin T assays of an incubated N-**[2.3.4.5.6F]Phe**-GAIL (3 mM) sample in ammonium acetate (10 mM) buffer.

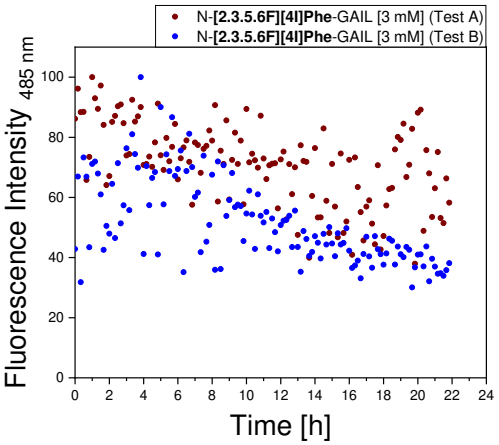

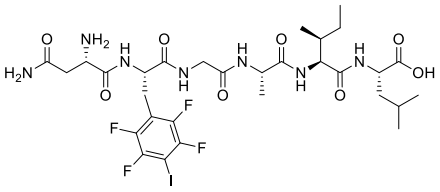

Figure S30: Two individual (brown and blue symbols) Thioflavin T assays of an incubated N-**[2.3.5.6F][4I]Phe**-GAIL (3 mM) sample in ammonium acetate (10 mM) buffer.

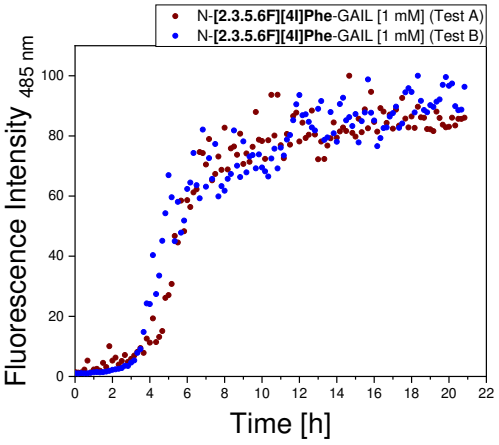

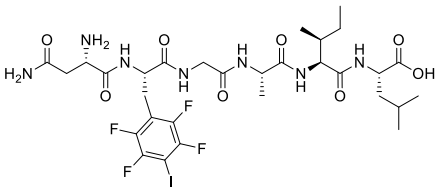

Figure S31: Two individual (brown and blue symbols) Thioflavin T assays of an incubated N-**[2.3.5.6F][4I]Phe**-GAIL (1 mM) sample in ammonium acetate (10 mM) buffer.

4. Additional TEM Micrographs of selected NFGAIL Sequences

N-[4F]Phe-GAIL [4 mM]

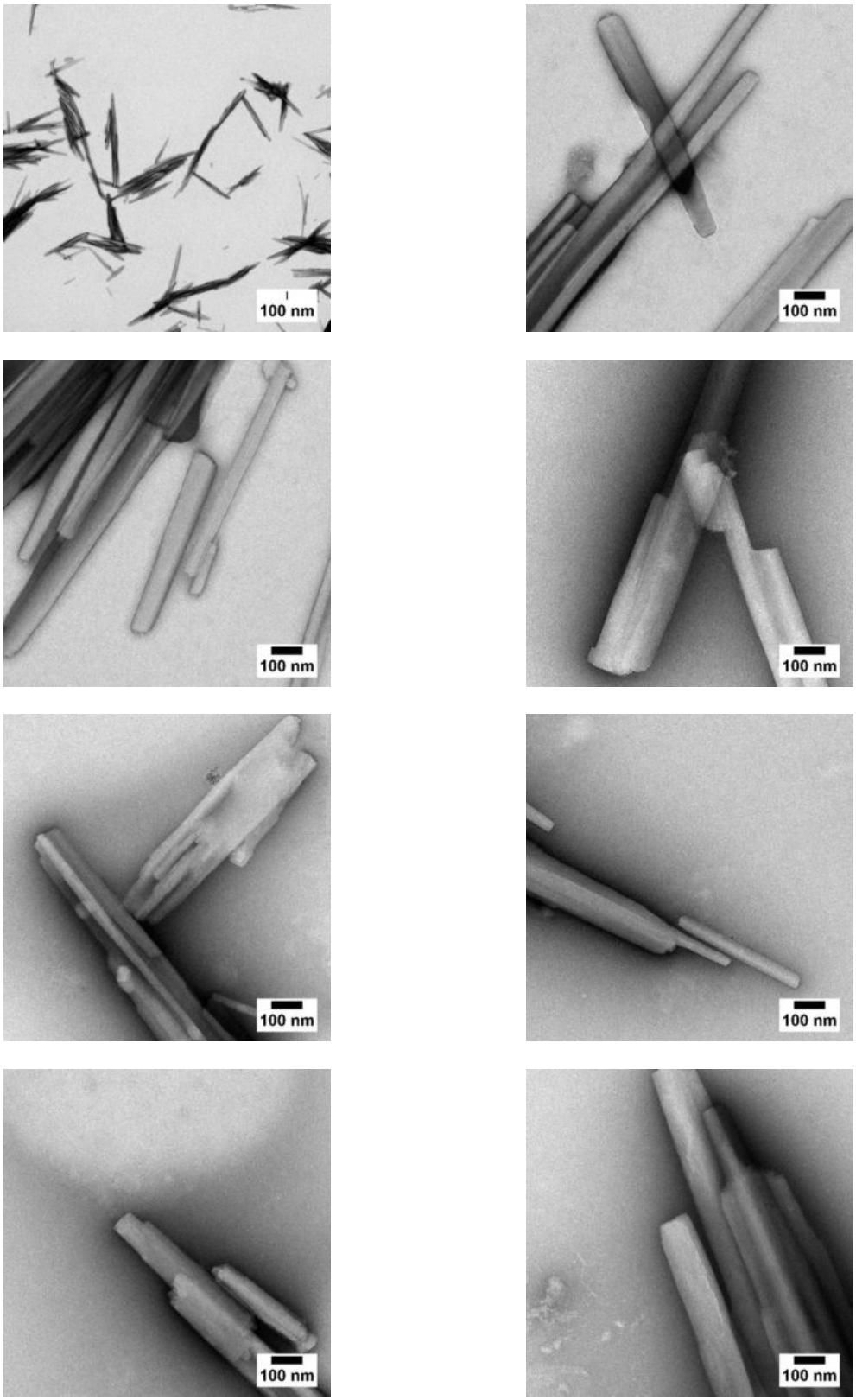

Figure S32: Negative staining transmission electron microscopy (TEM) images of N-**[4F]Phe**-GAIL [4 mM] in ammonium acetate buffer (10 mM, pH ~ 7).

N-[3.5F]Phe-GAIL [4 mM]

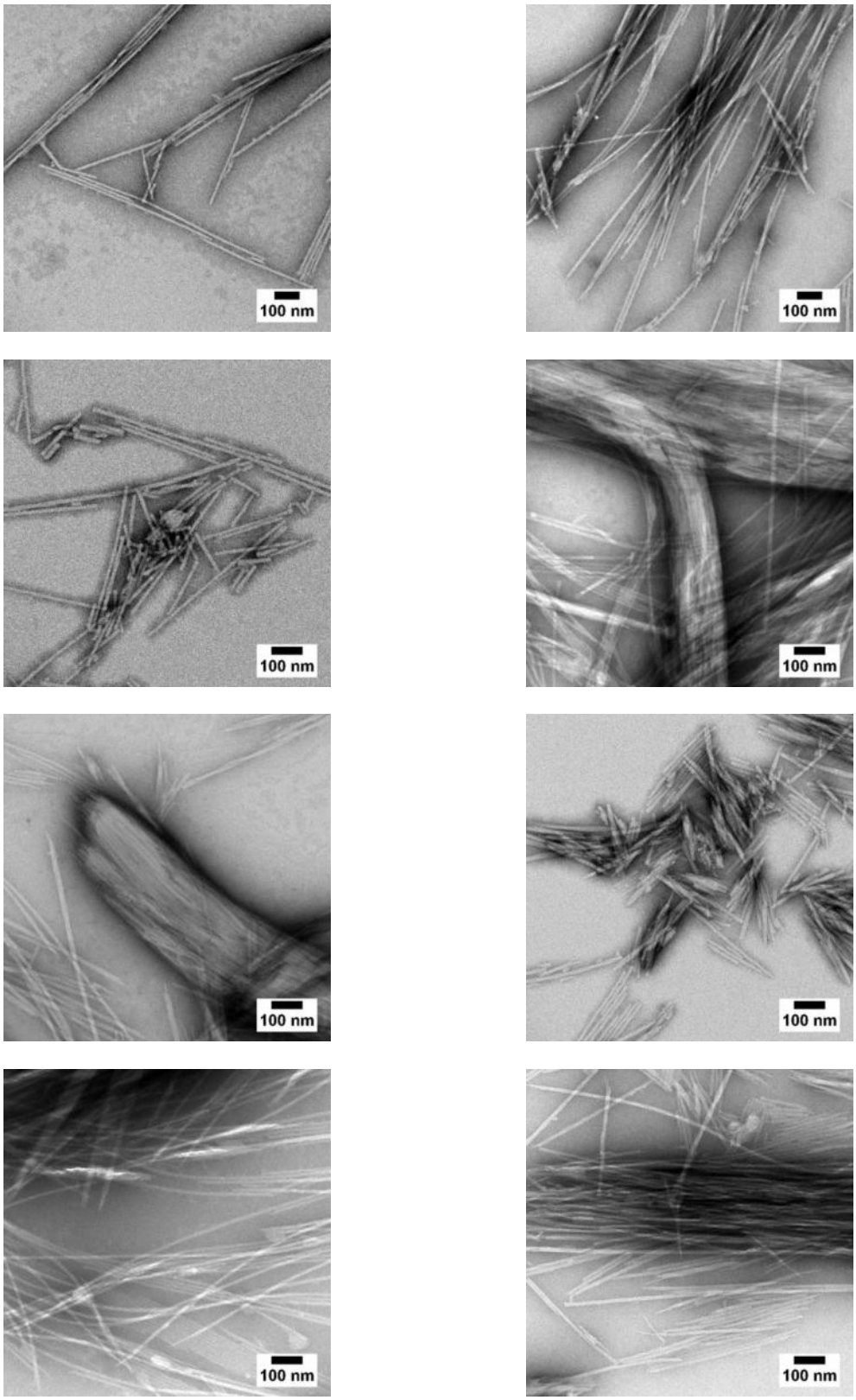

Figure S33: Negative staining transmission electron microscopy (TEM) images of N-**[3.5F]Phe**-GAIL [4 mM] in ammonium acetate buffer (10 mM, pH ~ 7).

N-[2.3.5.6F]Phe-GAIL [3 mM]

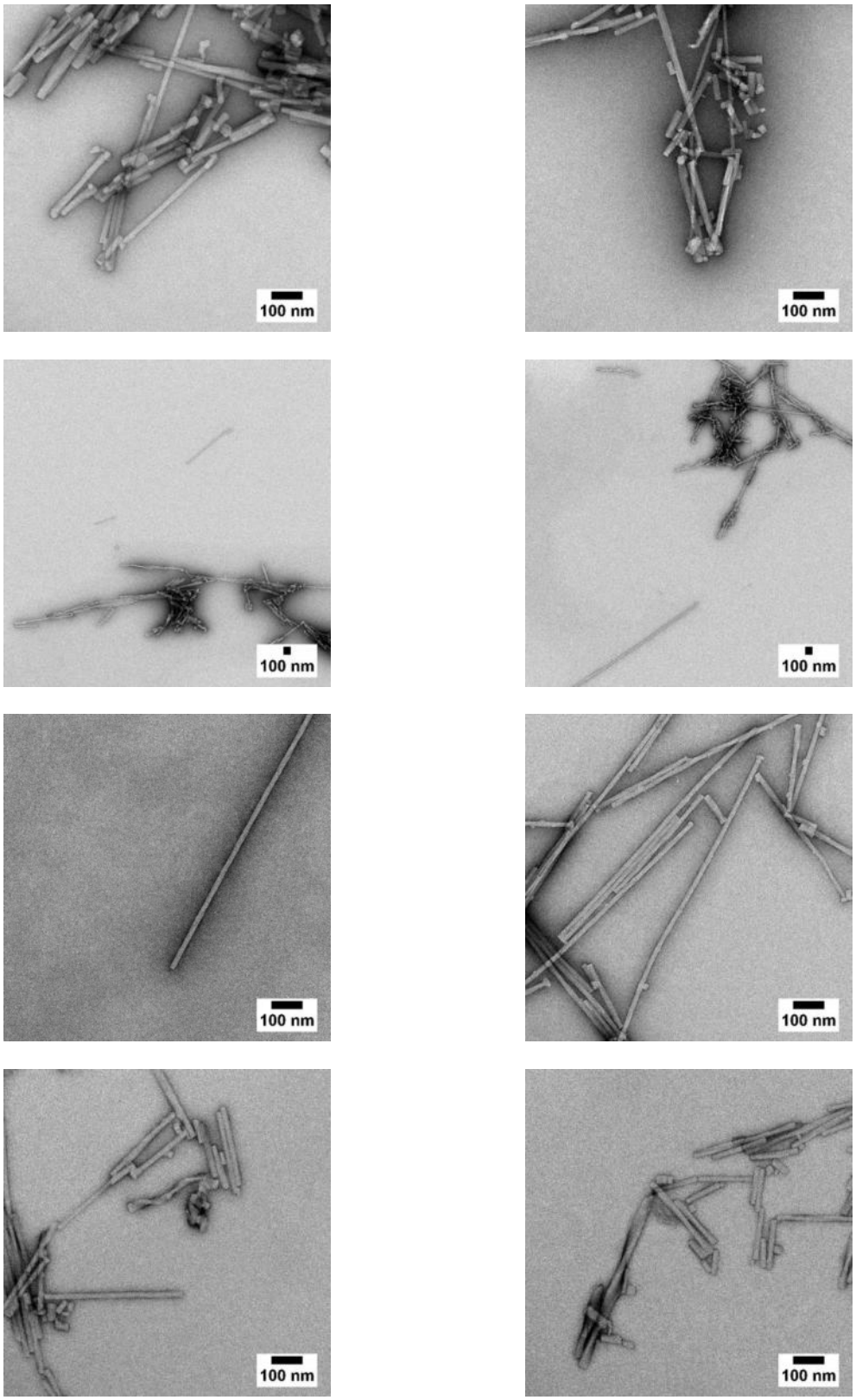

Figure S34: Negative staining transmission electron microscopy (TEM) images of N-**[2.3.5.6F]Phe**-GAIL [3 mM] in ammonium acetate buffer (10 mM, pH ~ 7).

N-[2.3.4.5.6F]Phe-GAIL [3 mM]

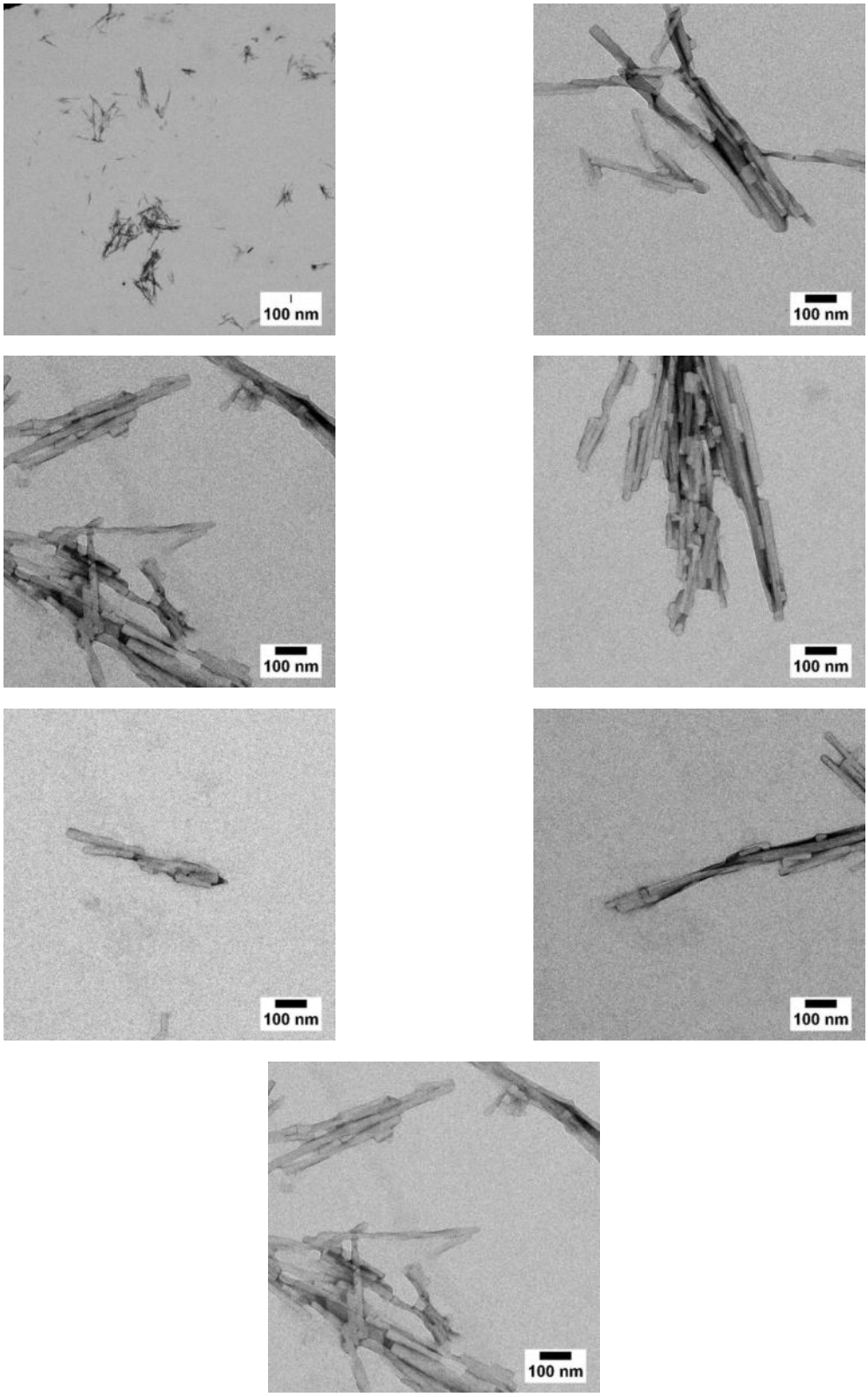

Figure S35: Negative staining transmission electron microscopy (TEM) images of N-**[2.3.4.5.6F]Phe**-GAIL [3 mM] in ammonium acetate buffer (10 mM, pH ~ 7).

N-[2.3.5.6F][4I]Phe-GAIL [1 mM]

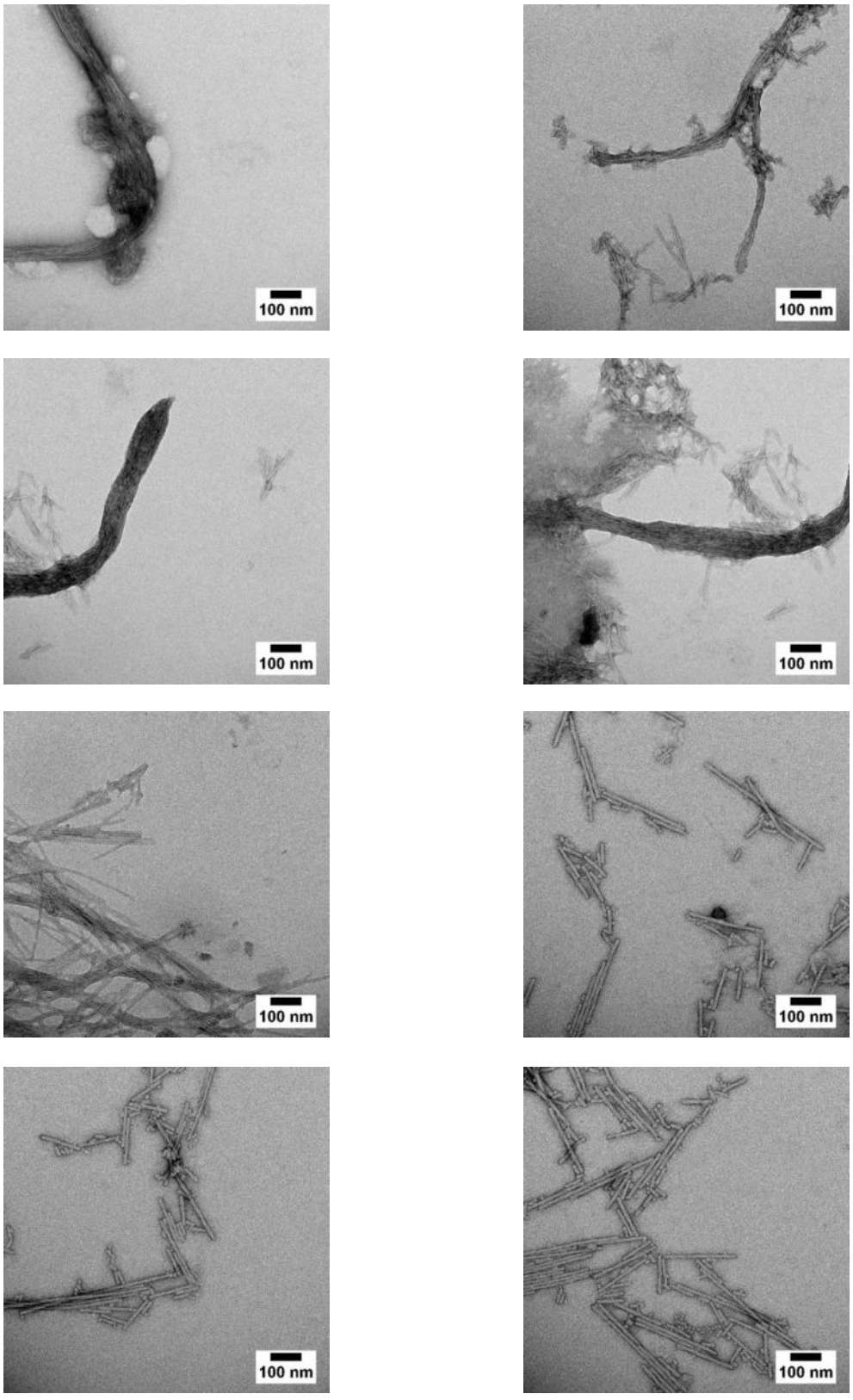

Figure S36: Negative staining transmission electron microscopy (TEM) images of N-**[2.3.5.6F][4I]Phe**-GAIL [4 mM] in ammonium acetate buffer (10 mM, pH ~ 7).

5. Small-Angle X-Ray Scattering of Peptide Aggregates NFGAIL

Results

Samples of peptide aggregates of the native NFGAIL sequence (4mM, **[N]**) and its fluorinated derivatives N-**[2.3.5.6F]Phe**-GAIL (3 mM, **[A]**) and N-**[2.3.4.5.6F]Phe**-GAIL (3 mM, **[B]**) were measured in solution with SAXS. The resultant scattering curves are shown in **Figure S8**. It can be seen, that the scattering intensities at low *q*-values decrease proportional to q^{-2}. (indicated by a straight line). This indicate a flat ribbon-like filament structure in which the length of the filaments is much larger than the cross-section dimensions. We found that the simplest structure model for data interpretation is a parallelepiped, which was applied, for example, to determine of the cross section of cyanobacterial actin filaments.[2] The scattering function of a parallelepiped with length *a*, widths *b* and thickness *c* with *a* > *b* > *c* is given by:[3]

$$I_1(q) = k_1 \int_0^{\pi/2} \left[\frac{\sin\left(\frac{1}{2} aq \sin\theta \cos\varphi\right)}{\frac{1}{2} aq \sin\theta \cos\varphi} \times \frac{\sin\left(\frac{1}{2} bq \sin\theta \sin\varphi\right)}{\frac{1}{2} bq \sin\theta \sin\varphi} \times \frac{\sin\left(\frac{1}{2} cq \cos\theta\right)}{\frac{1}{2} cq \cos\theta} \right] sin\theta d\theta d\varphi \qquad \textbf{(1)}$$

The best fits of eq. **(1)** to the data of aggregated NFGAIL samples are displayed in **Figure S8** (red solid curves). The filament's length is beyond the maximum size accessible and was therefore held constant at *a* = 1000 nm. The resultant values of the native NFGAIL sequence **[N]** and its fluorinated derivatives N-**[2.3.5.6F]Phe**-GAIL **[A]**, and N-**[2.3.4.5.6F]Phe**-GAIL **[B]** are shown in **Figure S9**.

In our study (see **Figure S9**) the thickness of the ribbons increases in the line c = 8.1 ± 0.2 nm **[A]**, 11.73 ± 1.2 nm **[B]**, 21.8 ± 0.1 nm **[N]**. The fibrils of the native NFGAIL sequence **[N]** display also the largest width of the ribbons (b = 54 ± 1 nm) but N-**[2.3.4.5.6F]Phe**-GAIL **[B]** has a larger width (44 ± 2 nm) than N-**[2.3.5.6F]Phe**-GAIL **[A]** (31 ± 2 nm). Therefore, the cross-section areas (estimated as product of b and c) of the fluorinated NFGAIL derivatives N-**[2.3.5.6F]Phe**-GAIL **[A]**, and N-**[2.3.4.5.6F]Phe**-GAIL **[B]** are similar (359 nm^2 and 365 nm^2), while the cross-section area of native NFGAIL **[N]** is much larger (1176 nm^2).

The structure model data are comparable to the values as published for a parallelepiped by Langkilde et al.[4]

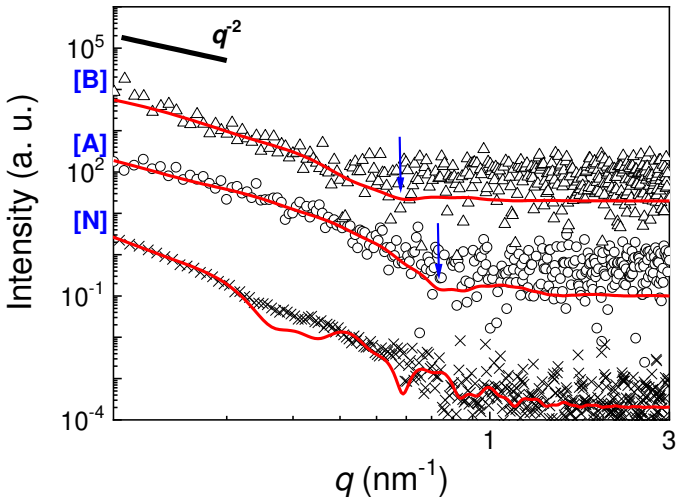

Figure S37: Small-angle scattering data of of the native NFGAIL sequence (4mM, **[N]**) and its fluorinated derivatives N-**[2.3.5.6F]Phe**-GAIL (3 mM, **[A]**) and N-**[2.3.4.5.6F]Phe**-GAIL (3 mM, **[B]**) and curve fits using a parallelepiped model (symbols and red solid line, respectively). Arrows indicate the position of the minima of the curves of samples **[A]** and **[B]**. The straight black line corresponds to a decay of the intensity proportional to q^{-2}. Curve were vertically shifted for better visibility.

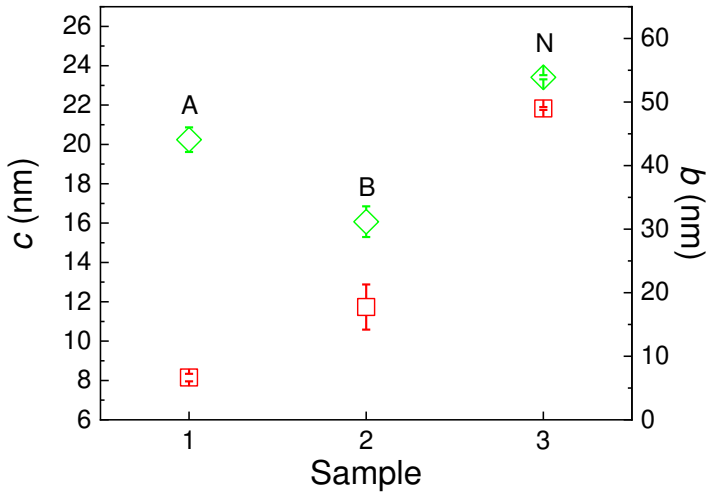

Figure S38: SAXS results for the native NFGAIL sequence (4mM, **[N]**) and its fluorinated derivatives N-**[2.3.5.6F]Phe**-GAIL (3 mM, **[A]**) and N-**[2.3.4.5.6F]Phe**-GAIL (3 mM, **[B]**) for the height (thickness), *c* , and width, *b*, of the filaments (red and green symbols, respectively) as derived from curve fits using the parallelepiped structure model.

6. References

[1] H. Zheng, K. Comeforo, J. Gao, *Journal of the American Chemical Society* **2009**, *131*, 18-19.

[2] aA. Guljamow, F. Delissen, O. Baumann, A. F. Thünemann, E. Dittmann, *PloS one* **2012**, *7*, e29926-e29926; bJ. S. Pedersen, *Advances in Colloid and Interface Science* **1997**, *70*, 171-210.

[3] aP. Mittelbach, *Acta Phys. Austriaca* **1961**, *14*, 185-211; bA. Kuchibhatla, A. S. A. Rasheed, J. Narayanan, J. Bellare, D. Panda, *Langmuir* **2009**, *25*, 3775-3785.

[4] A. E. Langkilde, K. L. Morris, L. C. Serpell, D. I. Svergun, B. Vestergaard, *Acta crystallographica. Section D, Biological crystallography* **2015**, *71*, 882-895.